



**HAL**  
open science

# Chains of magnetosomes with controlled endotoxin release and partial tumor occupation induce full destruction of intracranial U87-Luc glioma in mice under the application of an alternating magnetic field

Edouard Alphan ery, Ahmed Idbah, Clovis Adam, Jean-Yves Delattre, Charlotte Schmitt, Fran ois Guyot, Im ene Chebbi

## ► To cite this version:

Edouard Alphan ery, Ahmed Idbah, Clovis Adam, Jean-Yves Delattre, Charlotte Schmitt, et al.. Chains of magnetosomes with controlled endotoxin release and partial tumor occupation induce full destruction of intracranial U87-Luc glioma in mice under the application of an alternating magnetic field. *Journal of Controlled Release*, 2017, 10.1016/j.jconrel.2017.07.020 . hal-01565231

**HAL Id: hal-01565231**

<https://hal.sorbonne-universite.fr/hal-01565231v1>

Submitted on 19 Jul 2017

**HAL** is a multi-disciplinary open access archive for the deposit and dissemination of scientific research documents, whether they are published or not. The documents may come from teaching and research institutions in France or abroad, or from public or private research centers.

L'archive ouverte pluridisciplinaire **HAL**, est destin ee au d ep ot et  a la diffusion de documents scientifiques de niveau recherche, publi es ou non,  emanant des  tablissements d'enseignement et de recherche fran ais ou  trangers, des laboratoires publics ou priv es.

1 **Chains of magnetosomes with controlled endotoxin release and partial**  
2 **tumor occupation induce full destruction of intracranial U87-Luc glioma**  
3 **in mice under the application of an alternating magnetic field.**

4 *Edouard Alphandéry<sup>a,b,\*</sup>, Ahmed Idbah<sup>c</sup>, Clovis Adam<sup>d</sup>, Jean-Yves Delattre<sup>c</sup>, Charlotte Schmitt<sup>c</sup>,*  
5 *François Guyot<sup>a</sup>, Imène Chebbi<sup>b</sup>.*

6

7 <sup>a</sup> Institut de minéralogie, de physique des matériaux et de cosmochimie, UMR 7590 CNRS, Sorbonne  
8 Universités, UPMC, University Paris 06, Muséum National d'Histoire Naturelle, 4 Place Jussieu, 75005,  
9 Paris, France.

10 <sup>b</sup> Nanobacterie SARL, 36 boulevard Flandrin, 75016, Paris, France.

11 <sup>c</sup> Inserm U 1127, CNRS UMR 7225, Sorbonne Universités, UPMC, University Paris 06, UMR S 1127,  
12 Institut du Cerveau et de la Moelle épinière, ICM, F-75013, Paris, France.  
13 AP-HP, Hôpitaux Universitaires Pitié Salpêtrière - Charles Foix, Service de Neurologie 2-Mazarin, F-  
14 75013, Paris, France.

15 <sup>d</sup> Laboratoire de neuropathologie, GHU Paris-Sud-Hôpital Bicêtre, 78 rue du Général Leclerc, 94270 Le  
16 Kremlin Bicêtre, France.

17

18 \*Corresponding author Email address:

19 [edouardalphandery@hotmail.com](mailto:edouardalphandery@hotmail.com)

20

21

22

23 **ABSTRACT**

24 Previous studies have shown that magnetic hyperthermia could efficiently destroy tumors both  
25 preclinically and clinically, especially glioma. However, antitumor efficacy remained suboptimal and  
26 therefore required further improvements. Here, we introduce a new type of nanoparticle synthesized by  
27 magnetotactic bacteria called magnetosomes with improved properties compared with commonly used  
28 chemically synthesized nanoparticles. Indeed, mice bearing intracranial U87-Luc glioma tumors injected  
29 with 13  $\mu\text{g}$  of nanoparticles per  $\text{mm}^3$  of tumor followed by 12 to 15 of 30 minutes alternating magnetic  
30 field application displayed either full tumor disappearance (40% of mice) or no tumor regression using  
31 magnetosomes or chemically synthesized nanoparticles, respectively. Magnetosome superior antitumor  
32 activity could be explained both by the increased production of heat and by endotoxin release under the  
33 alternating magnetic field application. Most interestingly, this behavior was observed when  
34 magnetosomes occupied only 10% of the tumor volume, which suggests that an indirect mechanism,  
35 such as an immune activity, is involved in tumor regression. This is desired for the treatment of  
36 infiltrating tumors, such as glioma, for which whole tumor coverage by nanoparticles can hardly be  
37 achieved.

38

39

40 **KEYWORDS**

41 Magnetosomes, magnetotactic bacteria, magnetic hyperthermia, alternating magnetic field, glioblastoma.

42

43

44

45

## 47 1. INTRODUCTION

48 A series of different nanotechnologies, such as lipid-based nanoformulations, polymer-drug conjugates,  
49 recombinant viruses, metallic nanoparticles, drug-targeted antibodies, and herbal nanoparticles, have  
50 been successfully developed for cancer treatment both at fundamental and industrial levels (1). Among  
51 them, technologies in which nanoparticle anti-tumor activity can be controlled by applying an external  
52 source of energy, such as a laser (2), (3), radiation (4), (5), ultrasound (6), (7), or magnetic field (8), (9)  
53 appear promising because they can potentially enhance both treatment safety and efficacy. Strategies to  
54 increase nanoparticle SAR by combining magnetic hyperthermia with photothermia using magneto-  
55 plasmonic nanohybrids have also been suggested (10), (11). There is interest in developing this type  
56 of nanotechnology for glioblastoma (GBM) treatment, especially for the most severe GBM cases, which  
57 are non-operable. With the current standard of care, *i.e.*, maximal safe surgery, concurrent  
58 radiochemotherapy and adjuvant chemotherapy, GBM, which affects 25,000 patients per year in the  
59 United States and Europe (12), (13), remains incurable with a poor prognosis. The five-year survival  
60 time of patients with GBM is low at 10% (14), (15), demonstrating the need for new treatment  
61 options (16), (17), (18), (19), (20). Among the potential treatments for GBM are different types  
62 of nanothermotherapies (21), such as photodynamic therapy (22) and magnetic hyperthermia, which  
63 have been tested to treat GBM (9). Compared with other thermotherapies, magnetic hyperthermia (23),  
64 (24), (25), (26), (27), in which tumors are typically heated to 43-50 °C by intratumor  
65 administration of iron oxide nanoparticles followed by alternating magnetic field (AMF) application,  
66 appears promising. This is due to more localized heat produced by the nanoparticles, which results in  
67 enhanced efficacy, and to tumor destruction achieved at lower temperatures, which strengthens  
68 treatment safety. In a clinical trial that enrolled 14 patients with GBM, magnetic hyperthermia treatment  
69 performed using small chemically synthesized iron oxide nanoparticles (IONP) was well-tolerated by

70 patients, did not produce major side effects, and led to an increased survival time of 7 months compared  
71 with conventional treatments (28), (29).

72 Treatment efficacy could potentially be further improved by using chains of magnetosomes (CM), which  
73 are iron oxide nanoparticles synthesized by magnetotactic bacteria, instead of IONP. In previous studies,  
74 CMs have been shown to destroy MDA-MB-231 breast tumors subcutaneously xenografted under the  
75 skin of mice more efficiently than IONPs (30), (31). Magnetosome efficacy was attributed to the  
76 large magnetosome size, leading to stable ferrimagnetic properties and to a large amount of heat  
77 produced under AMF application, as well as to an arrangement of chains that prevented aggregation and  
78 promoted homogenous magnetosome distribution in the tumor (32), (33), (34), (35).

79 In the present study, anti-tumor activity against U-87-Luc GBM was studied both *in vitro* and *in vivo*  
80 with a suspension containing CMs. We first demonstrated that the amount of endotoxins released from  
81 the CMs can be controlled under AMF applications. CM cytotoxicity and internalization properties in  
82 the presence of U87-Luc cells were also studied *in vitro*. Mice bearing intracranial U87-Luc tumors  
83 were then treated under conditions that could be followed clinically, *i.e.*, using an AMF with 30 mT and  
84 198 kHz ( $H.f = 8 \cdot 10^8 \text{ A}\cdot\text{m}^{-1}\cdot\text{s}^{-1}$ , below the threshold of  $5 \cdot 10^9 \text{ A}\cdot\text{m}^{-1}\cdot\text{s}^{-1}$ , above which Eddy currents may  
85 occur) (26), (36). Treatment parameters, such as the number of magnetic sessions and quantity of  
86 CMs administered, that lead to complete disappearance of the intracranial U87-Luc tumors were  
87 determined and compared with IONP treatment, which has been previously used to perform preclinical  
88 magnetic hyperthermia tumor treatments (37), (38). During the various treatments, nanoparticle  
89 distribution in the tumors and the presence of different cell types in the brain were also examined by  
90 histology. This study also suggests a mechanism for tumor destruction and verified that the brain tumor  
91 disappeared fully following magnetic hyperthermia treatment with CMs.

## 92 **2. MATERIALS AND METHODS**

### 93 ***2.1. Preparation of the injectable CM suspension***

94 *Magnetospirillum magneticum* AMB-1 magnetotactic bacteria at biosafety level 1 were purchased from  
95 ATCC (79024 strain). Five milliliters of a suspension containing  $4.10^6$  of these bacteria per milliliter  
96 were introduced into one liter of sterile 1653 ATCC culture medium containing nutrients and additives,  
97 such as minerals, vitamins, and an iron source, as listed in the 1653 ATCC medium, which is required  
98 for the proliferation of these bacteria and for magnetosome production. The bottles were completely  
99 filled with sterile medium to prevent contamination by other bacterial species and to avoid a high  
100 oxygen concentration in the growth medium, which would prevent magnetosome production. The media  
101 containing the bacteria were then placed in an incubator at 30 °C for 7 days to enable bacterial growth  
102 and magnetosome production. After 7 days, the media was centrifuged at 4000 g for 45 minutes. The  
103 bacterial pellet was washed using 1 ml of sterile water (Millipore®). Magnetotactic bacteria were  
104 concentrated using a strong Neodinium magnet (0.6 Tesla), re-suspended in 0.05 M TRIS and sonicated  
105 with a sonicating finger at 0 °C for 2 hours at 30 W. The suspension containing the chains of  
106 magnetosomes extracted from the magnetotactic bacteria was washed several times with sterile water  
107 using a magnet to isolate the CMs from the supernatant containing cellular debris and residual bacteria  
108 until the cellular debris disappeared from the supernatant. Sonication was performed at 30 W by a series  
109 of three 2-second pulses between each wash. The CMs were then re-suspended in 1 ml of sterile water.  
110 For the intracranial injections, the CMs were re-suspended in a sterile injectable solution containing 5%  
111 glucose and exposed to ultraviolet lamp (UV) irradiation for 12 h for partial sterilization.

## 112 **2.2. Preparation of IONPs:**

113 IONPs, which are starch-coated iron oxide nanoparticles, were purchased from Micromod  
114 Partikeltechnologie GmbH company, Friedrich-Barnewitz-Str. 4, D-18119, Rostock, Germany (ref: 10-  
115 00-102).

## 116 **2.3. Nanoparticle Characterization:**

117 Nanoparticle sizes, shapes, and organization were determined using a transmission electron microscope  
118 (JEM-2100, JEOL, Japan). The iron concentrations of the different nanoparticle suspensions were  
119 measured by mixing these suspensions with hydrochloric acid and hydrogen peroxide to produce  $Fe^{3+}$

120 ions complexed with potassium thiocyanate, and total iron was then determined via an absorbance  
121 measurement at 476 nm. The concentrations were expressed as mg of maghemite contained in the CMs  
122 and IONPs per ml of suspension or per mm<sup>3</sup> of tumor. The zeta potentials of the different nanoparticles  
123 in suspension were measured by dynamic light scattering (DLS, ZEN 3600, Malvern Instruments, UK).  
124 The stability of the nanoparticle suspensions was estimated by measuring the changes in the optical  
125 densities of these suspensions, which were measured at 476 nm for 15 min. Nanoparticle FTIR spectra  
126 were recorded with a FTIR spectrometer (Vertex 70, Bruker, USA). The amount of organic material at  
127 the nanoparticle surface was measured using an elemental CHNS analyzer (Flash EA 1112, Thermo  
128 Fisher Scientific, USA). More details about each of these techniques are provided in the supplementary  
129 materials section.

#### 130 ***2.4. Set-up for generating the alternating magnetic field and for measuring the temperature***

131 We used an induction system operating at 198 kHz to generate the alternating magnetic field. Mice,  
132 Eppendorf tubes, petri dishes containing nanoparticles and possibly cells were inserted into a coil with a  
133 7-cm diameter with four spires to generate a magnetic field with an average strength of 30 mT. We used  
134 an infrared camera (EasIR-2, Optophase, France) positioned 20 cm above the coil to measure the  
135 temperature both *in vitro* and *in vivo*. We verified the temperature with a thermocouple positioned at the  
136 tumor center and that the infrared camera measured the temperature at the tumor center. This was  
137 possible due to the shallowness of the tumor.

#### 138 ***2.5. Amount of endotoxins released under AMF application***

139 Suspensions containing 2 µl of CMs or IONPs at a concentration of 20 mg/ml in iron oxide were treated  
140 as follows. Nanoparticle suspensions were exposed to 0, 1, 2, 3, and 4 magnetic sessions, during which  
141 an AMF of 198 kHz and average strength of 30 mT was applied for 30 minutes. After AMF  
142 applications, 100 µl of nonpyrogenic water was added to the suspensions, and the suspensions were  
143 mixed for one minute and centrifuged at 13 000 rotations per minute for 15 minutes. The endotoxin  
144 concentration of the supernatant was measured using the Limulus ameobocyte lysate (LAL) assay.

#### 145 ***2.6. Materials and cells culture***

146 U87-MG Luc human GBM cell lines, which were transduced with a luciferase gene, were obtained from  
147 Keith Ligon's lab and used in this study. After thawing, the U87-MG Luc adherent cells were cultivated  
148 at 37 °C in the presence of 5% CO<sub>2</sub> in Dulbecco's Modified Eagle Medium (DMEM) containing 10%  
149 fetal bovine serum (FBS). Once the cells reached confluence, the culture dishes were rinsed with Hank's  
150 Balanced Salt Solution (HBSS). The cells were then detached with trypsinization for 5 minutes at 37 °C  
151 in the presence of 5% CO<sub>2</sub>. The trypsin activity was stopped by the addition of medium containing FBS.  
152 The cellular concentration was then determined using a Malassez cell.

### 153 ***2.7. U87-Luc cytotoxicity in the absence of AMF using an MTT assay***

154 U87-Luc cytotoxicity studies were evaluated using an MTT assay. This technique measures the ability of  
155 mitochondrial enzymes to reduce 3-(4,5-dimethylthiazol-2-yl)-2,5-diphenyltetrazolium bromide to  
156 purple formazan crystals. Cells were seeded at a density of 10<sup>4</sup> cells per well in 96-well flat-bottom  
157 plates and incubated in completed culture medium for 24 h. Then, the U87-Luc cell medium was  
158 removed and replaced with 10% FCS-medium containing CMs or IONPs at varying concentrations  
159 ranging from 7.8 µg/ml to 1000 µg/ml in maghemite. After 24 h of incubation, the cells were washed  
160 with HBSS and incubated with 0.1 ml of MTT (2 mg/ml) for an additional 4 h at 37 °C. The insoluble  
161 product was then dissolved by the addition of 100 µl of isopropanol. The absorbance corresponding to  
162 the solubilized formazan pellets, which reflect the relative viable cell numbers, was measured at 540 nm  
163 using a microplate reader. We measured the absorbance at 540 nm for the cells with the nanoparticles  
164 without formazan blue and we have subtracted this signal from the signal for the cells with nanoparticles  
165 with formazan blue. The percent inhibition of cell proliferation, inhibition (%), was then estimated using  
166 the following formula: % inhibition =  $[1 - (OD_{TC}/OD_{UC})] \times 100$ , where OD<sub>UC</sub> is the optical density of the  
167 suspension of untreated cell, *i.e.*, cells that have been washed with PBS and have not been in the  
168 presence of nanoparticles, measured at 540 nm, and OD<sub>TC</sub> is the optical density of the suspension of  
169 treated cells, *i.e.*, nanoparticle suspensions that have been added to cells, measured at 540 nm. The  
170 percent inhibition of cell proliferation was plotted as a function of the nanoparticle concentration. The  
171 experiments were performed in triplicate.



## 172 **2.8. *In vitro* efficacy of hyperthermia**

173 A total of 500,000 U87-Luc cells were seeded in a Petri dish (35 mm) for 24 hours. Then, 2 ml of IONP  
174 and CM suspensions were added to the cells at different concentrations varying between 1 mg/ml, which  
175 is sufficient to induce an increase in temperature increase, and 40  $\mu\text{g/ml}$ , which corresponds to the  
176 maximum magnetosome concentration in the tumor, *i.e.*, 40  $\mu\text{g}$  of magnetosomes per  $\text{mm}^3$  of tumor.  
177 When the same amount of nanoparticles used, we observed an increase in the temperature in solution  
178 but not *in vitro*, possibly due to the lower concentrations *in vitro* (2 ml at 20  $\mu\text{g/ml}$ ) than in solution (2  
179  $\mu\text{l}$  at 20 mg/ml). Next, these assemblies were exposed (or not) to a 30 mT and 198 kHz AMF for 30  
180 minutes. The cells were then incubated with the nanoparticles for 24 h. The nanoparticle media was  
181 removed, and the cells were washed twice with cold PBS. We verified that there were no observable  
182 nanoparticle aggregates at the cell surface and that the nanoparticles were mostly internalized in cells by  
183 optical microcopy. It is possible that nanoparticles that were not observed with the optical microscope  
184 remained at cell surface, meaning that the measurement provides an estimate of the maximum quantity  
185 of internalized nanoparticles or the amount of nanoparticles internalized in cells or at the cell surface.  
186 Next, 250  $\mu\text{l}$  of trypsin were added to detach the cells, and then the culture media was mixed with cells.  
187 Following this *in vitro* treatment, the mixtures were centrifuged at 800 rpm for 7 minutes. The  
188 supernatant was removed and replaced with 100  $\mu\text{l}$  of annexin-binding buffer, 5  $\mu\text{l}$  of Alexa Fluor 488  
189 Annexin V for early apoptosis detection, and 1  $\mu\text{l}$  of propidium iodide at 100  $\mu\text{g/ml}$  for late apoptosis  
190 and necrosis detection. The mixtures were incubated at room temperature for 15 minutes. Then, 400  $\mu\text{l}$   
191 of annexin-binding buffer was added to this cell suspension and mixed gently. Ten microliters of this  
192 suspension were loaded into the sample slide and were inserted completely into a Countess™ II FL  
193 Automated Cell Counter (Thermo Fisher scientific), which was able to detect the Annexin and  
194 Propidium Iodide emissions. The percentages of necrotic and apoptotic cells were thus obtained.

## 195 **2.9. *Internalization of nanoparticles***

196 Following the *in vitro* treatments described in 2.7, the different mixtures were loaded into the sample  
197 slide and completely inserted into a Countess™ II FL Automated Cell Counter to count the cells. The

198 mixtures were then centrifuged, and the supernatant was removed and replaced with 286  $\mu\text{l}$  of  $\text{HNO}_3$   
199 (70%); the resulting treated mixtures were maintained at 4  $^\circ\text{C}$  for 24 h to lyse cells and dissolve the  
200 nanoparticles into free iron. Finally, 10 ml of filtered water was added to all the treated mixtures and the  
201 iron concentration was then determined using ICP-AES measurements. We deduced the average  
202 quantity of iron coming from the nanoparticles, which was internalized in each cell.

### 203 **2.10. *In vivo experiments***

204 *In vivo* experiments were performed following ethical guidelines and surgery was performed following  
205 the guidelines of the Institutional Animal Care and Use Committee (“Ethic committee Charles Darwin  
206 N°5”, project ethic number: 00764.03). Mice were fed and watered according to these guidelines and  
207 euthanized by cervical dislocation when their weights had decreased by more than 20% or when signs of  
208 pain, unusual posture or prostration were observed. At day 0 (D0), a cell suspension containing  $10^5$  U87-  
209 Luc cells per microliter was first inoculated into the brains of 7-week-old CD-1 female nude mice with a  
210 mean weight of 20 g from Charles River. To achieve the surgical procedure leading to cell implantation,  
211 the mice were first anesthetized with a mixture of ketamine (100 mg/kg) and xylazine (8 mg/kg). The  
212 mouse head was then fixed in a stereotactic frame, a craniotomy was performed at the fixed coordinates  
213 (0.2.0) and 2  $\mu\text{l}$  of a suspension containing  $2 \cdot 10^5$  U87-Luc cells were injected at the coordinates (0.2.2).  
214 Tumors grew for 8 days between D0 and D8. At D8, 7 different groups containing 10 mice each were  
215 treated as follows (Table S1(a)):

216 - Group 1 received a 30  $\text{mm}^3$  GBM at coordinates (0.2.2) mm and 2  $\mu\text{l}$  of an isotonic solution  
217 containing 5% glucose without any further treatment;

218 - Group 2 received a 5  $\text{mm}^3$  GBM at coordinates (0.2.2) mm and the same glucose solution as  
219 Group 1, followed by magnetic treatment consisting in 12 magnetic sessions (S) on D8 (S1), D9 (S2),  
220 D10 (S3), D15 (S4), D16 (S5), D17 (S6), D22 (S7), D23 (S8), D24 (S9), D29 (S10), D30 (S11), and  
221 D31 (S12);

222 - Group 3 received a 3  $\text{mm}^3$  GBM at coordinates (0.2.2) mm and a suspension containing 40  $\mu\text{g}$  of  
223 magnetosome chains in maghemite without any further treatment;

224 - Group 4 received a 3 mm<sup>3</sup> GBM at coordinates (0.2.2) mm and the same suspension as Group 3,  
225 followed by magnetic treatment consisting in 15 magnetic sessions on D8 (S1), D9 (S2), D10 (S3), D15  
226 (S4), D16 (S5), D17 (S6), D22 (S7), D23 (S8), D24 (S9), D29 (S10), D30 (S11), D31 (S12), D36 (S13),  
227 D37 (S14), and D38 (S15);

228 - Group 5 received a 25 mm<sup>3</sup> GBM at coordinates (0.2.2) mm and the same suspension as group 3,  
229 followed by 15 magnetic sessions on D8 (S1), D9 (S2), D10 (S3), D15 (S4), D16 (S5), D17 (S6), D22  
230 (S7), D23 (S8), D24 (S9), D29 (S10), D30 (S11), D31 (S12), D36 (S13), D37 (S14), and D38 (S15);

231 - Group 6 received a 5 mm<sup>3</sup> GBM at coordinates (0.2.2) mm and 40 µg of IONPs in maghemite  
232 without any further treatment; and

233 - Group 7 received in a 3 mm<sup>3</sup> GBM at coordinates (0.2.2) mm and the same suspension as Group  
234 6, followed by 12 magnetic sessions on D8 (S1), D9 (S2), D10 (S3), D15 (S4), D16 (S5), D17 (S6), D22  
235 (S7), D23 (S8), D24 (S9), D29 (S10), D30 (S11), and D31 (S12).

236 For the different groups of mice, the bioluminescence intensity emitted by the living tumor cells was  
237 measured on D7, D14, D21, D28, D35, D42, D49, D56 and D150.

238 During each magnetic session (S1 to S15), the mice were exposed to an AMF at an average strength of  
239 30 mT and a frequency of 198 kHz that was applied for 30 minutes.

#### 240 **2.11. Bioluminescence intensity and tumor volume measurements**

241 The mice were first anesthetized using isoflurane. The bioluminescence intensity was then measured  
242 using an IVIS Spectrum “*In Vivo Imaging System*” (PerkinElmer, Inc.) 10 minutes after intraperitoneal  
243 injection of 100 mg/kg of beetle luciferin potassium salt (Promega: E1605) in PBS, which reacts with  
244 luciferase to produce luminescent oxo-luciferin, (39), (40), (41). Images were analyzed with the  
245 living Image 4.0 software from Caliper, Life Sciences. The bioluminescence intensity at the tumor site  
246 was divided by the bioluminescence intensity measured in the flanks to remove the mouse auto-  
247 luminescence signal. Then, the relationship between tumor bioluminescence intensity and tumor volume  
248 was determined. For that, bioluminescence intensities were measured at D7, D14, D21, D28 and D35 in  
249 a series of living mice. The tumor volumes were deduced from surface measurements of several

250 horizontal histological sections positioned at various tumor heights, which were collected from mice  
251 euthanized on the same day at the BLI measurements. A linear relationship was observed between the  
252 logarithm of tumor bioluminescence intensity (BLI),  $\log(\text{BLI})$ , and the logarithm of the tumor volume  
253 expressed in  $\text{mm}^3$ ,  $\log(\text{volume}(\text{mm}^3))$ (Fig. S3). A linear coefficient of 1.4 was deduced by fitting the  
254 plot in Fig. S3 with a linear function, a value that agrees with previously reported values (40), (42),  
255 (43), (44).

### 256 **2.12. Representation of tumor volume variations and estimates of survival time**

257 The variations in tumor volume in time were represented in Tukey diagrams using the Kaleida Graph  
258 4.03 software. Mouse survival times are plotted using the Kaplan-Meier model method (45), (46).  
259 The statistical significance of the survival time between the different groups was evaluated using the log  
260 rank test. Parameters are expressed as the median with p-values (9).

### 261 **2.13. Temperature measurements**

262 Intratumor temperatures were measured as a function of time during the various treatments in living  
263 mice using an infrared camera (EasIRTM<sup>2</sup>, Optophase) placed 20 cm above the coil.

### 264 **2.14. Histological analysis**

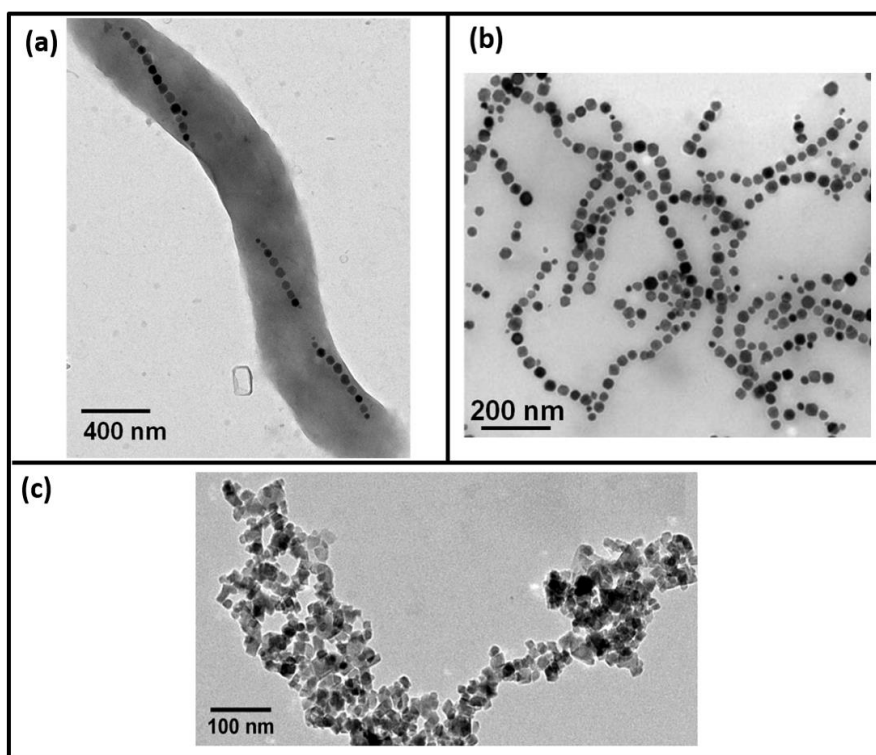
265 Histological studies were performed on extracted brains that were fixed with a 4% solution of  
266 formaldehyde for 24 hours, cut into 2-mm thickness transverse slices, washed in an ethanol (70%) bath  
267 for 12 hours and included in paraffin. Sections of paraffin blocks with a thickness of 4  $\mu\text{m}$  were  
268 deposited on glass slides and stained with hematoxylin-eosin (H&E) and/or Prussian blue to distinguish  
269 between healthy and tumor areas and to determine the location of the magnetosomes, polynuclear  
270 neutrophils (PNN), and tumor and healthy cells. Histological analysis was also performed on the mice  
271 that received glucose on day 8 and were euthanized 6 or 24 hours following glucose injection (Figs.  
272 S5(a) and S5(c)). Six mice were analyzed at various times, including after 1 magnetic session  
273 (Figs. S5(b)) or 24 hours after 3 magnetic sessions (Fig. S5(d)), in which they received CM on day 8 and  
274 were euthanized 4 hours (Figs. 9(a) and 9(c)) or 72 hours (Figs. 9(b) and 9(d)) after the CM injection;  
275 just after or 4 hours after 1 magnetic session (Figs. 8(a), 8(b) and 8(c)); and 24 hours after 3 magnetic

276 sessions (=72 hours, Figs. 8(d) to 8(g)), in which they received IONPs on day 8 and were euthanized 6  
277 or 72 hours after IONP administration (Figs. S4(a) and S4(c)) or 24 hours after 3 magnetic sessions (72  
278 hours (Figs. S4(b) and S4(d)).

### 279 3. RESULTS AND DISCUSSION

#### 280 3.1. Properties of CMs and IONPs used for the tumor magnetic hyperthermia treatments

281 CMs were extracted from AMB-1 whole magnetotactic bacteria, a species of bacteria that produces  
282 chains of nanoparticles called magnetosomes, as shown in the TEM image of a typical magnetotactic  
283 bacterium presented in Figure 1(a). After extraction from the magnetotactic bacteria, the magnetosomes  
284 maintain their organization in chains (Figure 1(b)), a type of organization that is advantageous for the  
285 treatment because it prevents aggregation and promotes uniform distribution and homogenous heat  
286 production. Magnetosomes appear to possess a cubooctahedric geometry, more uniform sizes and shapes  
287 than IONPs (Figs. S7(a) and S7(b)), a size that is larger than 20 nm for the majority of them and a mean  
288 size of ~45 nm (Fig. S1(a)), which leads to a coercivity  $H_c$  of ~200-300 Oe and a ratio between remnants  
289 and saturating magnetization of  $M_r/M_s \sim 0.35$  at physiological temperature (Fig. S6), (47).



290

291 **Figure 1:** Transmission electron microscopy images of (a) an AMB-1 *Magnetospirillum magnetotacticum* magnetotactic  
 292 bacterium, (b), chains of magnetosomes extracted from magnetotactic bacteria and (c) an IONP. Seven microliter suspensions  
 293 containing magnetotactic bacteria, chains of magnetosomes, and IONPs were deposited and dried on top of a carbon grid  
 294 before TEM observation.

295 Magnetosomes are composed of a core, which is made of iron oxide, as revealed by the FT-IR Fe-O  
 296 peak at 580 cm<sup>-1</sup> (table 1) and further determined to be maghemite by saturating isothermal remnant  
 297 magnetic measurements (47). The core is surrounded by a coating of organic material, including  
 298 phospholipids and lipopolysaccharides, as revealed by a series of FT-IR peaks [C=O at 1740 cm<sup>-1</sup>,  
 299 amide at 1650 cm<sup>-1</sup>, amine at 1530 cm<sup>-1</sup>, P=O at 1250 cm<sup>-1</sup>, and PO at 1050 cm<sup>-1</sup> (Table 1)]. The  
 300 coating, whose function is to bind magnetosomes together in chains (48), is estimated to be 1 to 5 nm  
 301 thick (Figure 1(b)) and to contain 13.9% carbon, as estimated by CHNS analysis. LAL measurements  
 302 further indicated that the organic material at the magnetosome surface is partially derived from  
 303 endotoxins whose concentration in CM suspensions is estimated as 1400-8400 EU per ml per mg of iron  
 304 oxide. Moreover, CM suspensions appear sufficiently stable to enable their *in vivo* administration, as  
 305 their absorption measured at 480 nm does not decrease by more than 30% within 20 minutes (Table 1).

		CM						IONP					
Endotoxin level (EU/mg/mL)		1400-8400						< 50					
% stability on water (iron concentration = 1mg/mL)		70						100					
Coating thickness (nm)		1 - 5						1					
Isoelectric Point (a.u)		4.2						9.5					
	pH	2	4	6	8	10	12	2	4	6	8	10	12
	ζ-Potential (mV)	20	2.5	-18	-26	-34	-38	7	6	6	5	3	-20
% C		13.9						8.7					
SAR (2μL, 40 μg of iron) (W/gFe)		Water			Brain			Water			Brain		
		57			4			10			0		
FT-IR (cm <sup>-1</sup> )		580	1050	1250	1530	1650	1740	610	1025		1150		
		Fe-O	P-O	P=O	N-H (amine)	N-H (amide)	C=O	Fe-O	C-O (alcohol)		C-O (ether)		

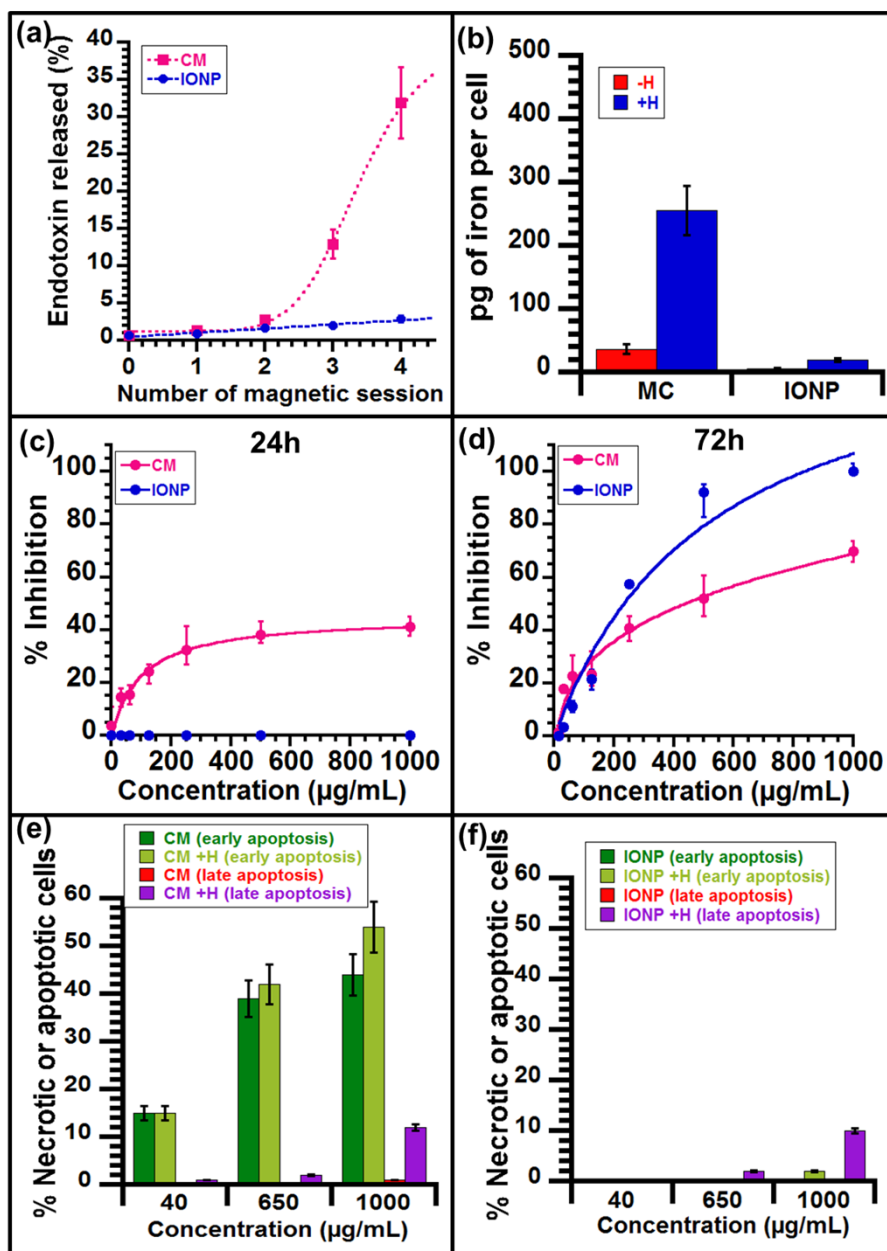
306  
 307 **Table 1:** The endotoxin content estimated in Endotoxin units (EU per mg in iron per ml), percent decreased absorption  
 308 measured at 480 nm in suspensions containing CM and IONP at a concentration of 1 mg in iron per ml after twenty minutes,  
 309 and estimates of the isoelectric point and zeta potential as a function of pH for suspensions containing CMs or IONPs.

310 Estimates of the coating thickness measured by transmission electron microscopy and percentage of carbon (% C) measured  
311 with CHNS and assignments from the different FT-IR peaks measured by FT-IR for the CM and IONP dried suspensions.  
312 Estimates of the specific absorption rates (SAR) in W per gram in iron for 2  $\mu$ l containing 40  $\mu$ g of CMs or IONPs in iron  
313 oxide mixed in water or introduced inside the mouse brains.  
314 Compared with CMs, IONPs are also ferromagnetic iron oxide nanoparticles but characterized by the  
315 following distinct features. Their geometric structure is parallelepipedic, they are not organized in chains  
316 and tend to form small aggregates as observed in the TEM image in Figure 1(c). IONPs are made of a  
317 core measuring  $\sim$ 19 nm by TEM (49), and whose composition is iron oxide as determined by FT-IR  
318 measurements that display an Fe-O peak at  $610\text{ cm}^{-1}$  (Table 1). The IONP core is surrounded by  
319 synthetic hydroxyethyl starch, as suggested by FT-IR and CHNS measurements performed on the  
320 IONPs, which shows FT-IR peaks at  $1150\text{ cm}^{-1}$  and  $1050\text{ cm}^{-1}$  that are attributed to hydroxyethyl starch  
321 ether and alcohol functional groups, and has a carbon percent of 8.7%, revealing the presence of an  
322 organic coating surrounding the inorganic iron oxide core (Table 1). Compared with CMs, the IONP  
323 surface contains a much lower endotoxin concentration of 50 EU per ml per mg of iron oxide, as  
324 measured with the LAL assay. Furthermore, IONPs are characterized by ferrimagnetic properties at  
325 physiological temperatures but at the following lower values: (1)  $H_c \sim 120\text{ Oe}$  and (2)  $M_r/M_s \sim 0.15$   
326 (49), (Fig. S6 and Table 1), which should yield lower SAR values. Furthermore, given that they are not  
327 less stable than CMs (Table 1) and that their anti-tumor efficacy has been demonstrated on tumor-  
328 bearing mice using magnetic hyperthermia (50), IONPs appear to be good standard for comparison to  
329 assess CM efficacy.

### 330 ***3.2. Under AMF applications, CM can release heat and an immune-stimulating substance more*** 331 ***efficiently than IONPs***

332 In an attempt to mimic the conditions in the *in vivo* treatments and to study the release of endotoxins  
333 from the CM and IONP surfaces in these conditions, we introduced 2  $\mu$ l of suspensions containing 40  
334  $\mu$ g of these nanoparticles in iron oxide at the bottom of a tube that we exposed to 1, 2, 3, and 4 magnetic  
335 sessions during which an AMF of 198 kHz and average strength 30 mT was applied for 30 minutes.  
336 During each of these 4 magnetic sessions, CM and IONP suspensions led to maximal temperatures

337 ( $T_{max}$ ) of 57 °C and 28 °C, respectively, after 3 minutes of AMF application (Fig. S2(a)). Specific  
 338 absorption rates (SAR) were deduced from the formula  $SAR=C_{water}(\Delta T/\delta t)/C_m$ , where  $\Delta T/\delta t$  are the  
 339 initial slopes of the plot in Fig. S2(a) [ $\Delta T/\delta t = 0.27$  °C/sec and 0.05 °C/sec for CM and IONP,  
 340 respectively],  $C_{water}= 4.2$  J/g.K is the specific heat capacity of water, and  $C_m = 0.02$  g/mL is the  
 341 concentration in iron oxide of the different nanoparticle suspensions. The SARs were estimated as  $57 \pm$   
 342  $6$  W/g<sub>Fe</sub> and  $10 \pm 3$  W/g<sub>Fe</sub> for CMs and IONPs, respectively. Therefore, the heating properties of CMs  
 343 appear far superior to those measured for IONPs.



344



345 **Figure 2:** (a) Percentage of endotoxin release from 2  $\mu$ l suspensions containing 40  $\mu$ g of CM or IONP in iron oxide that were  
346 exposed to 1, 2, 3 or 4 S with an AMF of 198 kHz and average strength of 30 mT applied for 30 minutes. (b) The quantity of  
347 iron released from MCs and IONPs, measured in pg and internalized per cell from U87-Luc cells incubated for 24 hours with  
348 1 mg/mL of CM or IONP in maghemite with(+H)/without(-H) AMF, where the AMF is the same as in (a). (c and d) The  
349 percentage inhibition of cell proliferation as a function of nanoparticle concentration for CMs and IONPs in maghemite in  
350 U87-Luc cells incubated for (c) 24 hours or (d) 72 hours with nanoparticle concentrations varied between 8  $\mu$ g/mL and 1  
351 mg/mL. (e and f) The percentages of late apoptotic (+ necrotic) and early apoptotic cell death as a function of nanoparticle  
352 concentration with(H)/without(-H) AMF where the AMF is the same as in (a) in U87-Luc cells incubated for 24 hours with  
353 (e) CM and (f) IONP at concentrations of 40  $\mu$ g/mL, 650  $\mu$ g/mL, and 1 mg/mL.

354 Moreover, the percentage of endotoxin release, which remains relatively similar at 1 to 3% during the  
355 first 2 magnetic sessions, strongly increased to 11% and 32% following the third and fourth magnetic  
356 sessions, respectively (Fig. 2(a)). This indicates that endotoxins, which are initially at the magnetosome  
357 surface, are progressively released from CMs under AMF application. Using CMs exposed to AMF, it  
358 therefore appears possible to simultaneously produce heat and release an immune-stimulating substance  
359 such as an endotoxin. Although endotoxins cannot be used in medicinal preparations, they may be  
360 replaced by a nontoxic equivalent, such as M-PLA, (51), (52). Combining the production of  
361 localized heat with the release of such a substance may possibly enhance antitumor efficacy. Compared  
362 with CMs, IONPs released a lower quantity of endotoxins and their percentage of endotoxin release did  
363 not exceed 5% between 1 and 4 S (Fig. 2(a)). Taken together, these heating and endotoxin release  
364 behaviors suggest that IONPs are less promising than CMs for the magnetic hyperthermia and endotoxin  
365 treatment in tumors.

### 366 ***3.3. CMs induce enhanced U87-Luc early apoptotic cell death and internalization in vitro***

367 In the absence of the AMF, *the* cytotoxicity of CMs towards U87-Luc cells was compared with that of  
368 IONPs using nanoparticle suspensions that were added to the cells and incubated for 24 and 72 hours at  
369 concentrations between 40  $\mu$ g/mL and 1 mg/mL. At 24 hours, the percent inhibition of cell proliferation  
370 increased with increasing nanoparticle concentrations from 0 to 40% for CM and remained at 0% for the  
371 IONPs (Figure 2(c)). At 72 hours, the percent inhibition increased more significantly for CMs, *i.e.*, from

372 0 to 60%, than for IONPs, *i.e.*, from 0 to 100% (Figure 2(d)). While CMs were observed to be more  
373 cytotoxic than IONPs at 24 hours, the opposite behavior was observed at 72 hours.

374 U-87-Luc cells were also incubated for 24 hours with CMs and IONPs at three different concentrations  
375 of 40, 650, and 1000  $\mu\text{g/ml}$  and then exposed to an AMF of 198 kHz and strength 47 mT for the first 30  
376 seconds and 30 mT for the remaining 29.5 minutes in an attempt to reach 41  $^{\circ}\text{C}$ , a temperature above  
377 which mild hyperthermia conditions are expected to occur (30). The 40 and 650  $\mu\text{g/ml}$  concentrations  
378 led to temperature increases of less than 2  $^{\circ}\text{C}$ , which were insufficient to reach the hyperthermia  
379 conditions. These concentrations resulted in necrosis and late apoptosis percentages that remained below  
380  $\sim 4\%$  with/without AFM for the CMs and IONPs and early apoptosis percentages that were similar  
381 with/without AFM at  $\sim 15\%$  and  $\sim 40\%$  for CMs at 40 and 650  $\mu\text{g/ml}$  in iron oxide, respectively, and at  
382 0% for IONPs (Figs. 2(e) and 2(f)). In contrast, at a concentration of 1 mg/ml, both CMs and IONPs  
383 yielded a more significant temperature increase of 7  $^{\circ}\text{C}$  up to 41  $^{\circ}\text{C}$  (Fig. S2(b)), which resulted in an  
384 increase in the necrotic and late apoptotic cell death percentages by 10%. These *in vitro* heating  
385 behaviors are In contrast, with those observed in solution, where CMs were observed to heat much more  
386 than IONPs.

387 The mechanisms of cellular death induced by CMs and IONPs were further examined. CMs appear to  
388 induce cellular death mainly through early apoptosis, with a percentage of early apoptotic cell death that  
389 increased with increasing CM concentrations from 15% at 40  $\mu\text{g/ml}$  to 50% at 1 mg/ml. Similar  
390 percentages were observed for CMs with/without AMF (Fig. 2(e)); this cell death mechanism was not  
391 observed with IONPs (Fig. 2(f)).

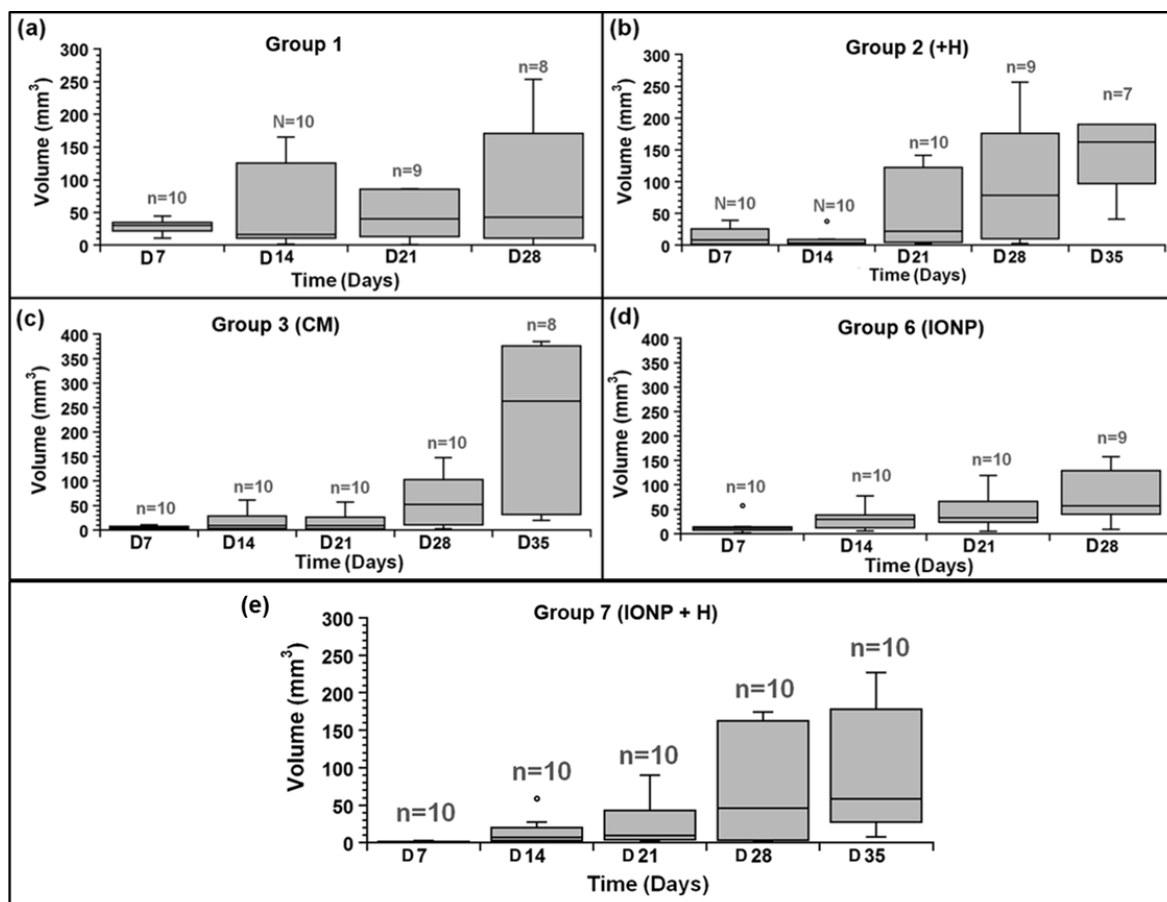
392 The differences in cell death mechanisms observed for IONPs and CMs as well as the more pronounced  
393 decrease in heating efficacy for CMs than IONPs observed between the *in vitro* and in suspension  
394 heating conditions may be explained by the different internalization properties. Indeed, the quantity of  
395 iron released from the nanoparticles, which are internalized in each cell, increased from 36.8 and 5.5 pg  
396 per cell without AMF application to 255.7 and 19.8 pg per cell with AMF application for the CMs and  
397 IONPs, respectively. It therefore appears that CMs are internalized better than IONPs and that the

398 internalization is enhanced by the presence of the AMF for both types of nanoparticles. This  
399 enhancement is more pronounced for CMs than for IONP by factors of 7 and 4, respectively (Figure  
400 2(b)). The different internalization properties for the CMs and IONPs may be explained by differences  
401 in their charges, *i.e.*, CM and IONP are negatively and positively charged at physiological pH,  
402 respectively (Table 1)); differences in organization, *i.e.*, CM and IONP are well-dispersed and tend to  
403 aggregate, respectively; and to larger values of coercivity for CMs (200-300 Oe) compared to IONPs  
404 (120 Oe) that may enhance CM magnetic field coupling. Furthermore, CM organization in chains may  
405 favor internalization by groups containing several magnetosomes (30), *i.e.*, potentially 6 for chains  
406 averaging 250 nm in length (Fig. S1(b), while IONPs may result in nanoparticles being internalized one  
407 by one or at a lower rate. The enhanced internalization of CMs may favor early apoptosis, which was  
408 previously observed with iron oxide nanoparticles, (53), and reduce its heating properties, possibly by  
409 preventing nanoparticle Brownian heating mechanisms (54).

#### 410 **3.4. CMs promote enhanced antitumor efficacy towards intracranial U87-Luc glioblastoma**

411 In the *in vivo* studies, mice receive the following treatment at the center of intracranial U87-Luc tumors:  
412 (1) glucose followed by treatment or not with magnetic sessions (groups 1 and 2), (2) 40  $\mu\text{g}$  of CMs or  
413 IONPs in maghemite without any further treatment (groups 3 and 6), (3) 40  $\mu\text{g}$  of CMs in maghemite  
414 followed by 15 magnetic sessions (groups 4 and 5), or (4) 40  $\mu\text{g}$  of IONPs in maghemite followed by 12  
415 magnetic sessions (group 7). The average size of the treated tumors was 3-5  $\text{mm}^3$ , except in group 5  
416 where it was 25  $\text{mm}^3$ . Following injection, the mice were exposed to 12 to 15 magnetic sessions, during  
417 which an AMF of 198 kHz and strength 30 mT was applied for 30 minutes (see Table S1(a) for a  
418 summary of the treatment conditions). In this study, U87 cells were labeled with the firefly luciferase  
419 gene to evaluate the changes in tumor volumes following the treatments via tumor bioluminescence  
420 intensity (BLI) measurements using the relationship between BLI and tumor volumes that we  
421 established (Fig. S3) (40), (42), (43), (44). For the mice belonging to the different groups without  
422 any measurable production of heat (groups 1, 2, 3, 6, and 7), Figures 3(a) to 3(e) show that the tumor  
423 volumes increased following tumor cell implantation without any signs of antitumor activity. Mice

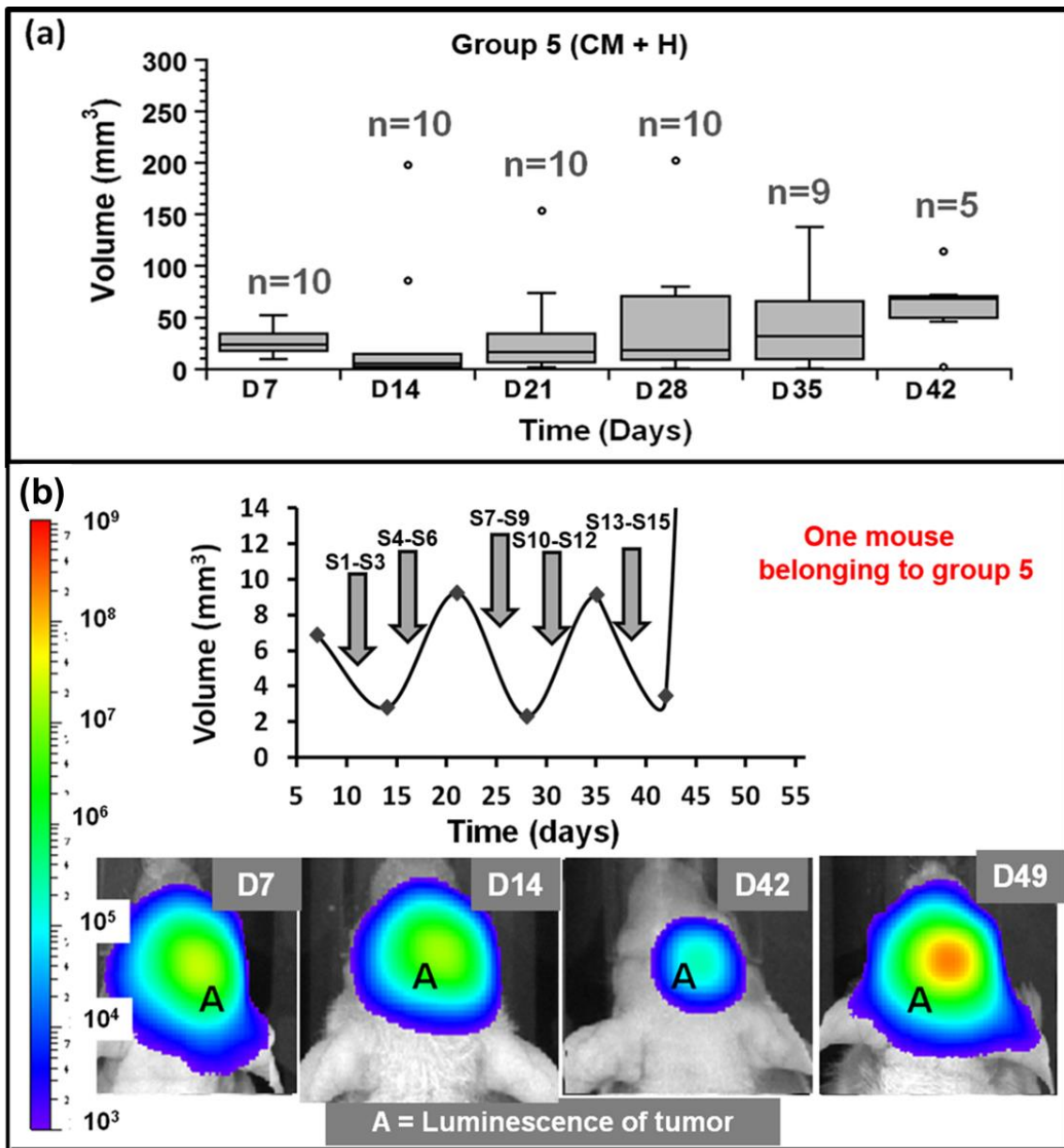
424 belonging to these groups were rapidly euthanized between days 28 and 42, leading to a rather low  
 425 median survival time of 42 to 46 days. In contrast, in the mice belonging to groups with heated tumors  
 426 (groups 4 and 5), antitumor activity is clearly observed and is more pronounced in the small (group 4)  
 427 than in the large (group 5) treated tumors.



428

429 **Figure 3:** Variations in tumor volumes as a function of time during the days following U87-Luc tumor cell implantation at  
 430 D0 for (a) untreated mice (group 1), (b) mice exposed to 15 magnetic sessions (group 2, +H), mice receiving a suspension  
 431 containing either (c) 40  $\mu\text{g}$  of CMs in iron oxide at the site of tumor cell implantation (group 3) or 40  $\mu\text{g}$  of IONPs in iron  
 432 oxide (group 6, IONP), or (e) 40  $\mu\text{g}$  of IONPs in iron oxide and exposed to 15 magnetic sessions. These variations are plotted  
 433 using Tukey diagrams, where error bars designate the maximum and minimum tumor volume values, circles represent single  
 434 tumor values, lower and upper horizontal rectangular sides designate lower and upper quartiles, respectively, and horizontal  
 435 lines within each box plot represents median tumor volumes. The number of living mice used to draw each box plot (n) is  
 436 also indicated above each box plot.

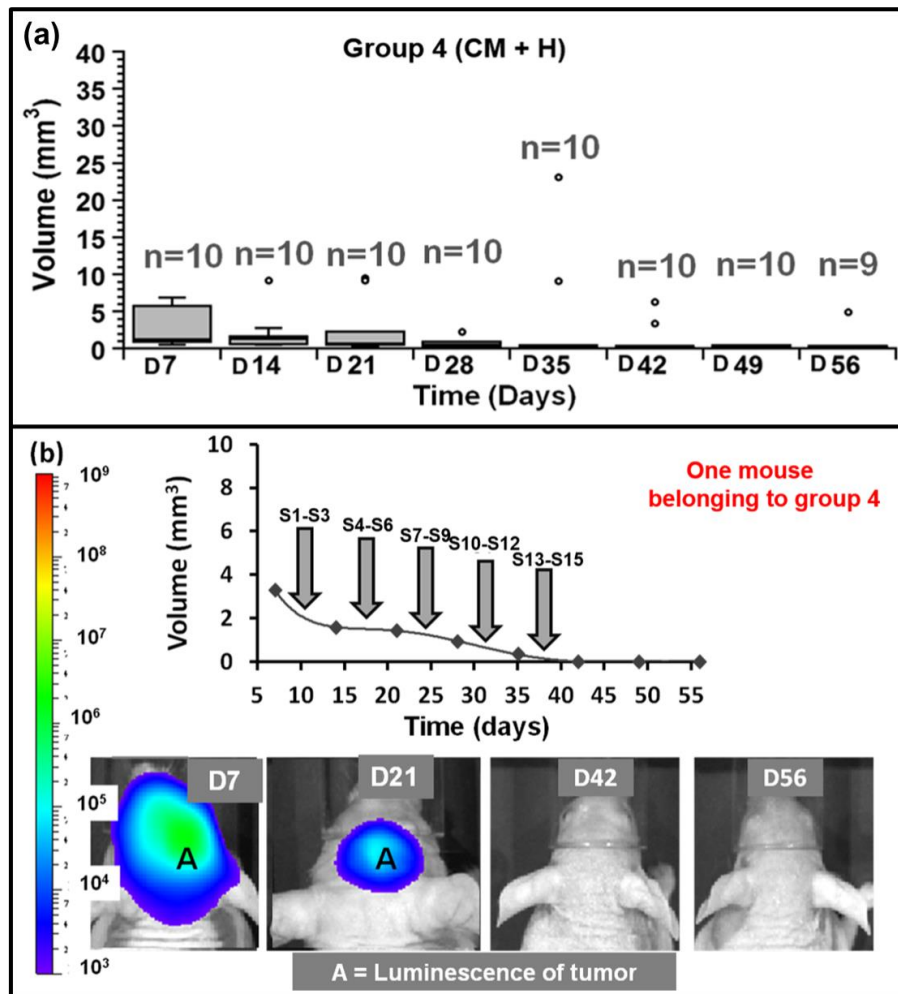
437 Figures 4(a) shows that tumor growth is delayed in group 5 with a median tumor volume that first  
 438 decreases from 25 mm<sup>3</sup> at day 7 to 5 mm<sup>3</sup> at day 14 and then increases from 5 mm<sup>3</sup> at day 14 to 70 mm<sup>3</sup>  
 439 at day 42. The behavior of a typical mouse belonging to this group is shown in Figure 4(b), which shows  
 440 three tumor volume oscillations (decrease followed by increase). This suggests that AMF application  
 441 causes repetitive anti-tumor activity without preventing tumor regrowth after 15 magnetic sessions. This  
 442 therapy led to a survival time of 49 days, which is only slightly increased compared to the unheated  
 443 groups.



444

445 **Figure 4:** (a) Variations in tumor volumes as a function of time during the days following U87-Luc tumor cell implantation at  
 446 D0 for mice receiving a suspension containing 40  $\mu\text{g}$  of CMs in iron oxide. The tumors reach an average volume of 25  $\text{mm}^3$   
 447 at D7 and were treated with 15 magnetic sessions (group 5, CM+H). (b) Variations in tumor volume and bioluminescence  
 448 intensity as a function of time during the days following tumor cell implantation in a mouse in group 5 with a tumor volume at  
 449 D7 of  $\sim 7.5 \text{ mm}^3$  that received 40  $\mu\text{g}$  of a suspension of CMs in iron oxide on D7 followed by 15 magnetic sessions (S1 to  
 450 S15).

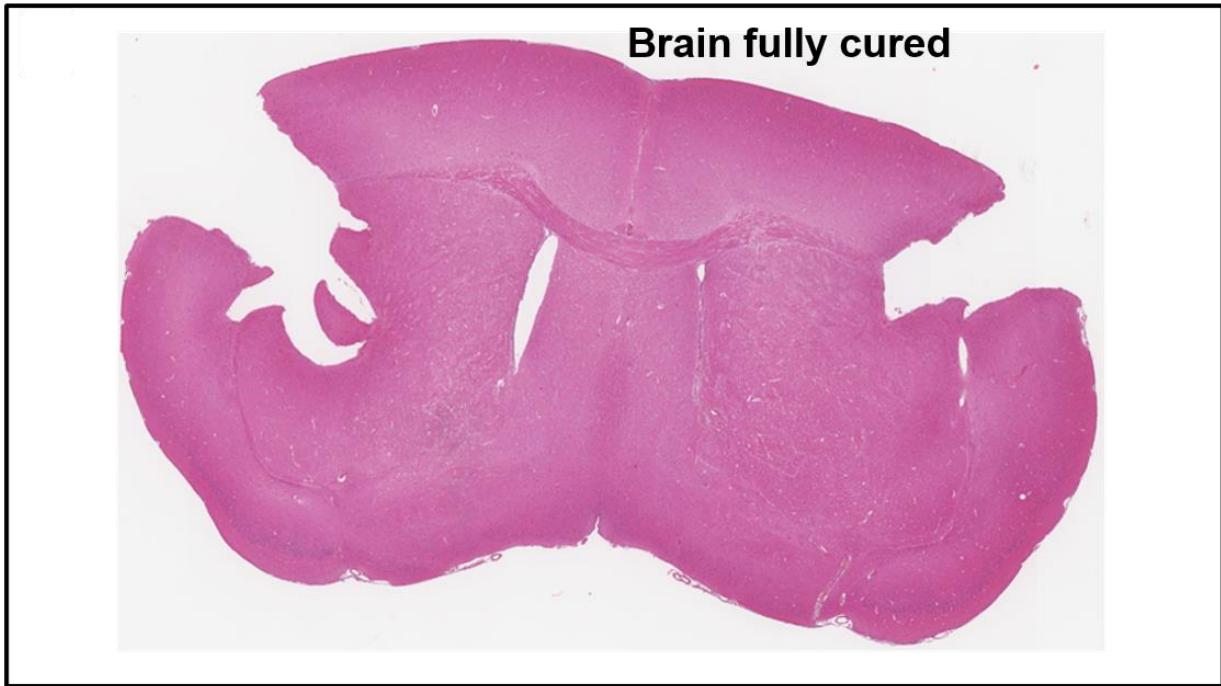
451 Figure 5(a) shows more significant antitumor activity in group 4 with full tumor disappearance at day 35  
 452 without tumor regrowth following 1 to 15 magnetic sessions. For a typical mouse belonging to this  
 453 group, Figure 5(b) shows the gradual decrease in the tumor volume following 1 to 15 magnetic sessions  
 454 until full tumor disappearance at day 40 without tumor regrowth. Compared with the unheated groups,  
 455 group 4 had the highest survival at 90 days (p-value < 0.0001).



456

457 **Figure 5:** (a) Variations in tumor volumes as a function of time during the days following U87-Luc tumor cell implantation at  
458 D0 for mice receiving a suspension containing 40  $\mu\text{g}$  of CMs in iron oxide when the tumors reach an average volume of 3  
459  $\text{mm}^3$  at D7 followed by 15 magnetic sessions (group 4, CM+H). (b) Variations in tumor volume and bioluminescence  
460 intensity as a function of time during the days following tumor cell implantation for a mouse belonging to group 4 with a  
461 tumor volume at D7 of  $\sim 3 \text{ mm}^3$  that receiving 40  $\mu\text{g}$  of CMs in iron oxide on D7 followed by 15 magnetic sessions (S1 to  
462 S15).

463 On day 150, 40% of the mice from this group were still alive without any unusual behaviors. Then, the  
464 mice were euthanized and slides of their brains from the tumor cell implantation region were imaged by  
465 optical microscopy, revealing the absence of tumors or tumor lesions and a brain neuronal structure  
466 identical to that of a healthy brain (Figure 6). These results suggest that the tumors had fully disappeared  
467 in these mice. Further analysis of mice from group 4 suggests that treatment does not result in any  
468 healthy tissue damage. Indeed, it can be deduced from the optical microscopy images of the brain  
469 sections from mice treated with CM with/without AMF collected at different times ranging from 4 hours  
470 to 150 days after CM administration (Figs. S4(a) to S4(d), S5(a) to S5(d) and Figs. 8(a) to 8(g), 9(a) to  
471 9(d)) that healthy tissues in the hippocampus and brain do not contain lesions or edema. Such  
472 observations can be explained by an LPS-activated neuro-protective response by the microglia (55).  
473 Thus, the treatment of the mice in group 4 appears safe and fully efficient.



474

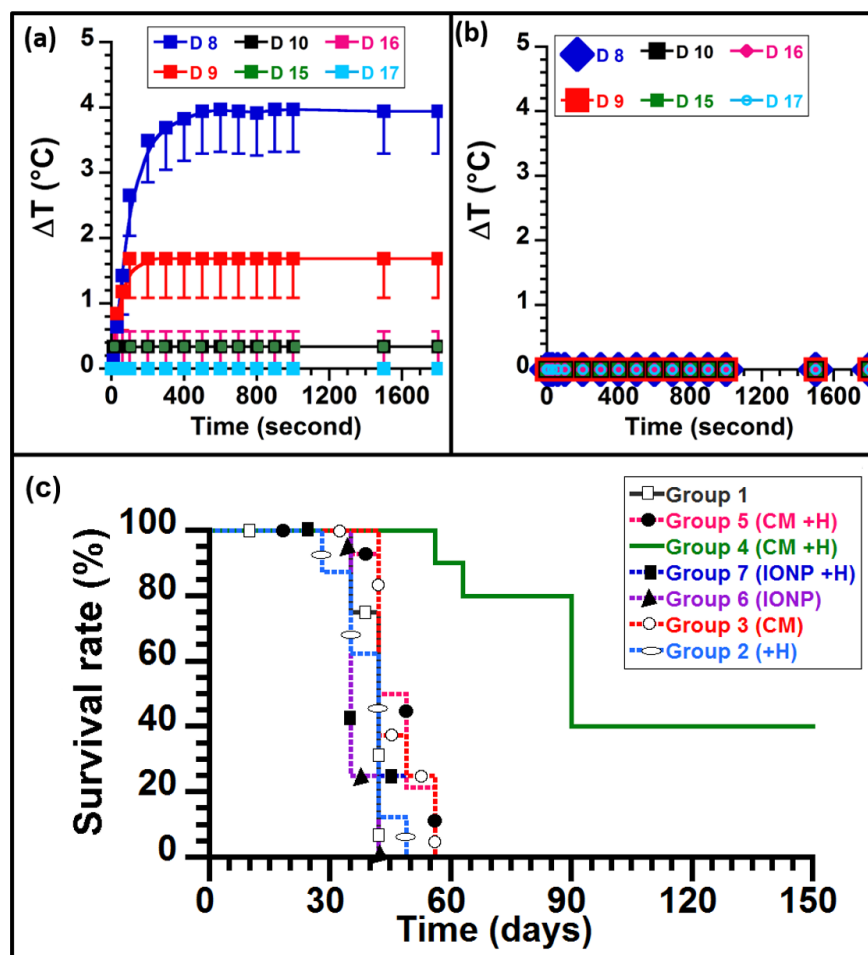
475 **Figure 6:** Optical microscopy image of a 4- $\mu\text{m}$ -thick brain section stained with hematoxylin and eosin from a mouse in group 4 that  
476 received 40  $\mu\text{g}$  of CMs in iron oxide followed by 15 magnetic sessions. This mouse was euthanized 7 months after  
477 magnetosome administration. No tumor was observed in this brain section.

478

### 479 ***3.5. Distribution of CMs in the tumor favors in vivo heating during the various S***

480 CM led to temperature increases of 4  $^{\circ}\text{C}$  at D8 (S1), 1.7  $^{\circ}\text{C}$  at D9 (S2), 0.4  $^{\circ}\text{C}$  at D10, D15 and D16 (S3,  
481 S4, S5) and then constant temperatures after D17 (Figures. 7(a) and 7(b)).



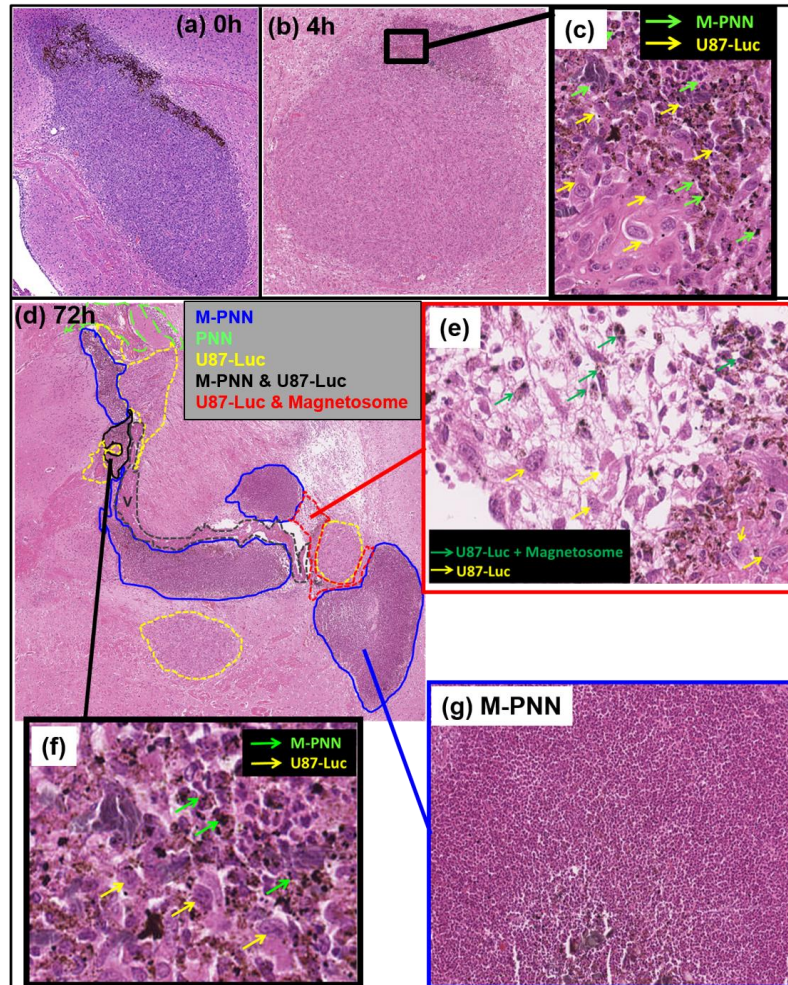


482

483 **Figure 7:** (a), Temperature increases above  $28.5^{\circ}\text{C}$  observed during each magnetic session ( $\Delta T$ ) on D8, D9, D10, D15, D16  
 484 and D17 in the mice from groups 4 and 5 treated with CMs. (b) The same as in (a) for the mice in group 7 treated with  
 485 IONPs. After D17, tumor temperature increases were no longer observed. (c) Variations in mouse survival times as a function  
 486 of time during the days following U87-Luc tumor cell implantation for mice with the following treatments: (1) untreated  
 487 (group 1), (2) exposed to 15 magnetic sessions (group 2), (3) treated with suspensions containing  $40\ \mu\text{g}$  of CMs in iron oxide  
 488 without magnetic sessions (group 3), (4) treated with  $40\ \mu\text{g}$  of CMs in iron oxide in  $\sim 3\ \text{mm}^3$  tumors followed by 15 magnetic  
 489 sessions (group 4), (5) administered  $40\ \mu\text{g}$  of CMs in iron oxide in  $\sim 25\ \text{mm}^3$  tumors followed by 15 magnetic sessions (group  
 490 5), (6) administered  $40\ \mu\text{g}$  of IONPs in iron oxide (group 6), and administered  $40\ \mu\text{g}$  of IONPs in iron oxide followed by 15  
 491 magnetic sessions (group 7).

492 The rather limited increases in temperature under AMF, which are less pronounced than in the  
 493 capillaries (Fig. S2(a)), may be explained by the effects of AMF on CM distribution. Indeed, the tumor  
 494 occupation percentage decreases from  $\sim 50\%$  right after CM administration without AMF at D8 (Figs.  
 495 9(a) and 9(b)) down to 8-15% on D8 and D11 after 1 and 3 magnetic sessions, respectively, (Figs. 8(a),

496 8(b) and 8(d)). These percentages were estimated by delineating the regions containing the CMs and the  
497 tumors and by measuring the ratio between the surfaces of these two regions. Moreover, the decrease in  
498 CM heating properties over time may be attributed to internalization of CMs in U87 tumor cells, which  
499 was observed at 24 hours after 3 magnetic sessions (Fig 8(d) and 8(e)).



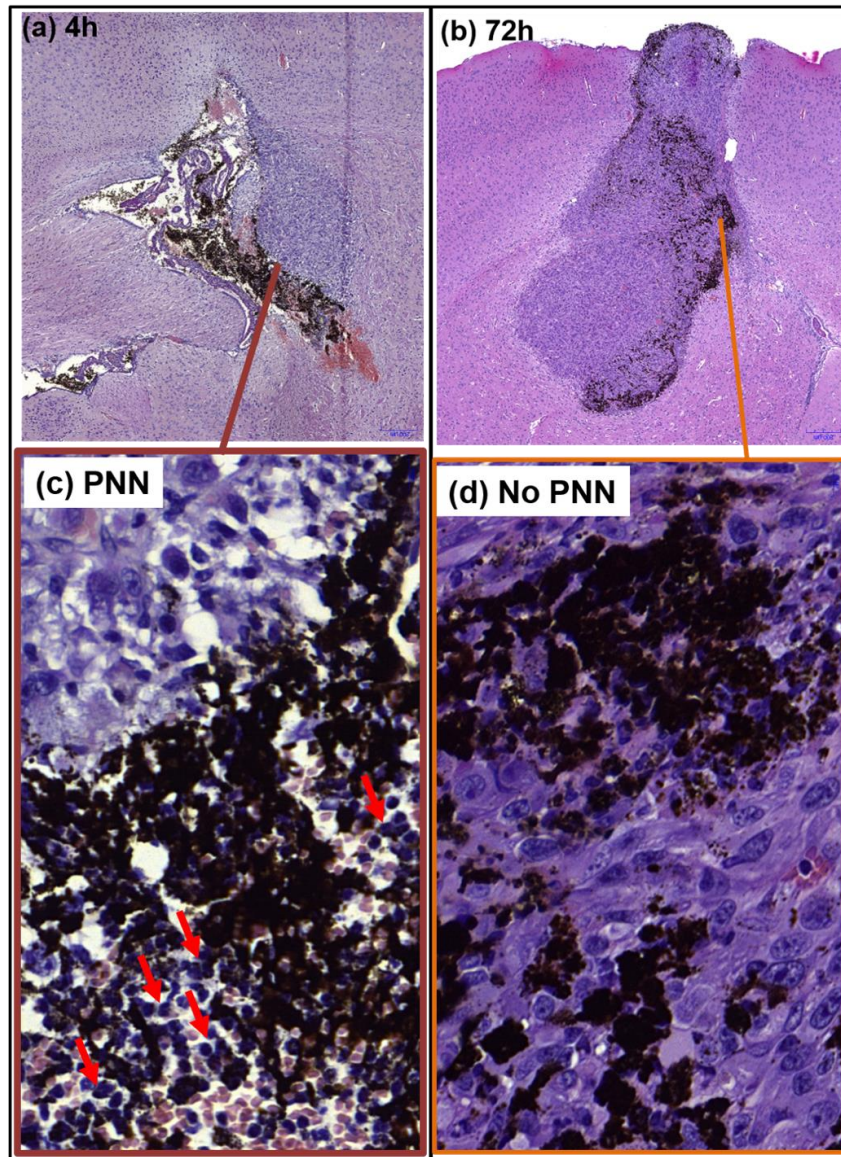
500

501 **Figure 8:** Optical microscopy images of 4  $\mu\text{m}$  thick brain sections stained with hematoeosin from mice receiving 40  $\mu\text{g}$  of  
502 CMs in iron oxide and exposed to (a-c) one or (d-g) three magnetic sessions. The mice were euthanized (a) 0 hours (0 h), (b  
503 and c) 4 hours (4 h), or (d-g) 72 hours (72 h) after MC administration with either (a-c) one or (d-g) three magnetic sessions.  
504 (c) An enlargement of the region in (b). The red arrows in (c) designate polynuclear neutrophils. (e), (f), and (g) are  
505 enlargements of three different regions from (d). PNN, M-PNN, U87-Luc, M-PNN & U87-Luc, and U87-Luc &  
506 magnetosomes designate polynuclear neutrophils, magnetosomes colocalized with polynuclear neutrophils, U87-Luc cells,  
507 magnetosomes colocalized with polynuclear neutrophils and U87-Luc cells, and U87-Luc cells colocalized with  
508 magnetosomes, respectively. The regions containing these different cells are surrounded in (d), while individual cells are  
509 indicated by arrows in (c), (e) and (f).

510 In contrast with CMs, IONPs do not produce any heat *in vivo* under the same excitation conditions. This  
511 behavior can be explained by their lower concentration in the tumor under AMF applications, *i.e.*, they  
512 are observed at the tumor surface as well as part of the tumor periphery at 6 hours (Figs. S4(a) and  
513 S4(c)); their more rapid diffusion in the ventricles, *i.e.*, IONPs and CMs localize in the ventricles at 6  
514 and 72 hours, respectively, (Figs. S4(a) and S4(b), Figs. 8(d)); and their earlier internalization in tumor  
515 U87-Luc and healthy BETZ brain cells, *i.e.*, IONPs and CMs are internalized at 6 and 72 hours,  
516 respectively, (Figs. S4(c) and S4(d), Fig. 8(e)). The combination of a low concentration in the tumor  
517 together with rather low SAR may undermine the IONPs' heating power, as was observed *in vivo*.

### 518 ***3.6. CM exposed to AMF activate PNN, which are possibly involved in antitumor activities***

519 Previous studies have reported that immune cells, such as dendritic cells, natural killers, and B and T  
520 cells, may participate in tumor destruction following hyperthermia treatment (56). Here, we examined  
521 potential involvement of other types of immune cells, *i.e.*, polynuclear neutrophils (PNN), which have  
522 only rarely been associated with antitumor activities (57), (58). While PNNs were not detected after  
523 glucose (Fig. S5) or IONP (Fig. S4) administration with/without magnetic sessions, we observed that  
524 these cells were localized at the same sites as the magnetosomes, forming a complex designated M-PNN  
525 in the mouse euthanized 4 hours after CM administration with/without magnetic sessions (Figs. 8(b),  
526 8(c), 8(d), 8(f), 8(g), 9(a) and 9(c)). More precisely, M-PNNs designate assemblies of magnetosomes  
527 and PNNs where the magnetosomes are less than 1  $\mu\text{m}$  away from the PNNs. The number of M-PNNs  
528 was estimated as 14000-19000 per  $\text{mm}^2$  4 hours after CM administration (Table S2). Because PNNs are  
529 known to be recruited by endotoxins (59), this behavior could be attributed to the endotoxins  
530 surrounding the magnetosome mineral core that attract PNN. Seventy-two hours later, the M-PNNs had  
531 disappeared in the absence of AMF (Figs. 9(b) and 9(d) and Table S2) but were detected in large  
532 quantities of 27,500 per  $\text{mm}^2$  (Table S2) after 3 magnetic sessions either within the tumor periphery  
533 (Fig. 8(d) and 8(f)) or in the tumor (Figs. 8(d) and 8(e)).



534

535 **Figure 9:** Optical microscopy images of 4  $\mu\text{m}$  thick brain sections stained with hematoeosin from mice receiving 40  $\mu\text{g}$  of  
 536 CMs in iron oxide without magnetic sessions and euthanized (a) 4 hours (4 h) or (b) 72 hours (72 h) after magnetosome  
 537 administration. (c) and (d) are enlargements of two regions in (a) and (b), respectively. PNN are observed in (c) and indicated  
 538 by red arrows, but not in (d).

539 These interesting behaviors might suggest that in the absence of AMF, endotoxins are progressively  
 540 deactivated, perhaps due to magnetosome internalization followed by magnetosome and endotoxin  
 541 decomposition. However, in the presence of AMF, the endotoxins are re-activated, possibly through the  
 542 release of endotoxins from the magnetosome surface, a behavior that perfectly fits with the observations  
 543 in solution (Fig. 2(a)) and/or via the destruction of cells in which magnetosomes are initially internalized  
 544 before AMF application. M-PNN complexes may have two main functions. First, they may be involved

545 in tumor destruction, as they are observed in the tumor region and Toll-like receptor (TLR) from the  
546 treated mice could be activated and trigger antitumor activity; this was previously reported for mice  
547 bearing B16 tumors (60). Second, they may also be involved in magnetosome capture and re-  
548 distribution. Indeed, after one and three magnetic sessions, magnetosomes and PNNs alone are rarely  
549 observed in the entire brain, including the tumor regions (Figs. 7(b) and 7(d)), and M-PNNs appear to be  
550 located either in the tumor, near the tumor periphery or in the ventricles (Figs. 7(b) and 7(c)). These  
551 results suggest that PNNs progressively migrate in the region where the magnetosomes are located  
552 between 0 and 4 hours after CM administration to form M-PNN complexes and that these complexes  
553 carry the magnetosomes from the inside to the outside of the tumor, possibly through the ventricle blood  
554 vessels. This behavior further agrees with the absence of heat production after D17, which suggests that  
555 magnetosomes have left the tumor by this date and/or have been dissolved into free iron. This idea is  
556 also in line with the well-known function of PNNs, which is to remove bacterial residues (61), (62).  
557 Magnetosome progressive departure from the tumor, possibly followed by magnetosome redistribution  
558 within the mouse, could be appealing for the treatment by preventing crystallized magnetosomes from  
559 remain in the brain for too long a period of time. Optimum treatment conditions correspond to those  
560 where magnetosomes remain in the brain long enough to perform the treatment, but not for too long, to  
561 avoid unnecessary long-term magnetosome interactions with brain tissues. These conditions may be  
562 identified by controlling PNN activation and M-PNN complex formation under AMF application.

### 563 ***3.7. CMs appear to destroy glioblastoma tumors more efficiently than chemically synthesized*** 564 ***nanoparticles under AMF applications***

565 Using the same quantity of nanoparticles administered, we have shown in this study that CMs lead to  
566 40% of mice with full tumor disappearance, while IONPs do not yield any observable antitumor  
567 activities. This result agrees with previous animal studies performed on mice and rats bearing GBM  
568 using intratumor administration of chemically synthesized nanoparticles exposed to AMF that did not  
569 improve survival (63) or increased survival by 15 days without resulting in a full cure (64), (26). In  
570 addition to being more efficient, magnetosomes could also be used in a lower quantity, thus

571 strengthening treatment safety. Indeed, the quantity of magnetosomes necessary to eradicate U87-Luc  
572 GBM in this study, which was 1 to 13  $\mu\text{g}$  in maghemite per  $\text{mm}^3$  of tumor volume, is much less than 60  
573  $\mu\text{g}$  per  $\text{mm}^3$  of tumor volume, which produced less-efficient anti-tumor activities with chemically  
574 synthesized nanoparticles (9).

#### 575 **4. CONCLUSION**

576 We demonstrated that 40% of mice bearing intracranial U87-Luc tumors displayed full tumor  
577 disappearance after intratumor administration of 40  $\mu\text{g}$  of CMs followed by 12 to 15 magnetic sessions,  
578 during which an AMF of average strength 30 mT and frequency 198 kHz was applied for 30 minutes. In  
579 contrast, similar antitumor efficacy was not observed when mice were treated with the same conditions  
580 and administered chemically synthesized nanoparticles instead of magnetosomes. Furthermore, the  
581 absence of mouse brain damage during and following the various treatments appears to indicate that a  
582 safe treatment could be performed with magnetosomes, provided that the endotoxins are replaced with  
583 an equivalently active but nonpyrogenic substance such as M-PLA. Antitumor activity does not appear  
584 to be dominated by nanoparticle cytotoxicity, as the CMs, which are more efficient than IONPs *in vivo*,  
585 do not enhance cytotoxicity towards U87-Luc cells compared with IONPs. Moreover, nanoparticle  
586 administration without AMF does not produce any observable anti-tumor effects. Instead, tumor  
587 destruction appears to be due to the heat produced by the CMs under AMF application, as the only mice  
588 that displayed clear anti-tumor effects had their tumors heated (groups 4 and 5). Under heating  
589 conditions, tumor tissue destruction may be caused by irreversible cell damage; cytolysis; actin filament,  
590 microtubule or mitochondrial dysfunction; DNA replication or RNA synthesis inhibition; or DNA  
591 polymerase denaturation (65), but these mechanisms seem insufficient to fully explain the observed  
592 antitumor activities. Indeed, tumor destruction does occur when the magnetosomes occupy a small  
593 percentage of the total tumor volume (~10%), suggesting that magnetosomes occupying the tumor can  
594 induce the destruction of the entire tumor. We have identified the following three possible mechanisms  
595 that could be responsible for full tumor destruction:

- 596 i) Early apoptosis, as apoptotic cell death is observed to be dominant *in vitro* for CMs and heat was  
597 previously shown to favor apoptotic cell death (65), (66), (67);
- 598 ii) Microvascular damage due to the presence of magnetosomes in the ventricles that possibly leads  
599 to the destruction of the blood vessels supplying the tumor with oxygen, which was previously reported  
600 to occur during hyperthermia, (68), and could possibly occur because CMs were observed in the  
601 ventricles near the blood vessel; and
- 602 iii) the involvement of PNN, which were previously reported to be involved in antitumor activity,  
603 (58) and were attracted by the magnetosomes in the tumor region due to the presence of endotoxins at  
604 magnetosome surface.
- 605 Finally, our study also suggests a method to control magnetosome distribution by attracting PNNs to the  
606 magnetosome region, which promotes the formation of magnetosome/PNN complexes that may  
607 progressively remove magnetosomes from the tumor through the ventricle blood vessels and enable their  
608 elimination. This process appears to be governed by the application (or not) of an AMF.

## 609 **ACKNOWLEDGMENTS**

610 We would like to thank the Eurostars Program (Nanoneck-2, E9309), subvention AIR from the region of  
611 Paris (A1401025Q), the ANRT, the ANR (Méfisto project), the French Research Tax Credit Program,  
612 Paris Biotech Santé, BPI, the University Paris 6, the University Paris XI, Marianne Labussière and Elvis  
613 Dervishi, as well as all other people and structures in France and Europe that have helped us and been  
614 supportive and enthusiastic about our research activities.

## 615 ***Abbreviations***

616	GBM	glioblastoma
617	AMF	alternating magnetic field
618	IONP	iron oxide nanoparticles
619	CM	magnetosome chains

620	UV	irradiation of an ultraviolet lamp
621	LAL	limulus ameocyte lysate
622	DMEM	Dulbecco's Modified Eagle Medium
623	FBS	fetal bovine serum
624	HBSS	Hank's Balanced Salt Solution
625	S	magnetic sessions
626	BLI	bioluminescence intensity
627	H&E	hematoxylin-eosin
628	PNN	polynuclear neutrophils
629	SAR	specific absorption rates
630	TLR	toll like receptor
631	M-PNN	PNN were localized at the same site as magnetosomes

632 **REFERENCES**

- 633 1. E. Alphan ery, P. Grand-Dewyse, R. Lef evre, C. Mandawala, M. Durand-Dubief, Cancer  
634 therapy using nanoformulated substances: scientific, regulatory and financial aspects. *Expert Review of*  
635 *Anticancer Therapy*. 15 (2015) 1233–55.
- 636 2. D.P. O’Neal, L.R. Hirsch, N.J. Halas, J.D. Payne, J.L. West, Photo-thermal tumor ablation in  
637 mice using near infrared-absorbing nanoparticles. *Cancer Letters*. 209 (2004) 171–6.
- 638 3. I.H. El-Sayed, X. Huang, M.A. El-Sayed, Selective laser photo-thermal therapy of epithelial  
639 carcinoma using anti-EGFR antibody conjugated gold nanoparticles. *Cancer Lett*. 239 (2006) 129–35.
- 640 4. X.Y. Su, P.D. Liu, H. Wu, N. Gu, Enhancement of radiosensitization by metal-based  
641 nanoparticles in cancer radiation therapy. *Cancer Biol Med*. 11 (2014) 86–91.
- 642 5. S. Her, D.A. Jaffray, C. Allen, Gold nanoparticles for applications in cancer radiotherapy:  
643 Mechanisms and recent advancements. *Advanced Drug Delivery Reviews*. (2015) *in Press*  
644 <http://dx.doi.org/10.1016/j.addr.2015.12.012>.



- 645 6. O.K. Kosheleva, T.C. Lai, N.G. Chen, M. Hsiao, C.H. Chen, Selective killing of cancer cells by  
646 nanoparticle-assisted ultrasound. *Journal of Nanobiotechnology*. (2016) 14:46.
- 647 7. Y. You, Z. Wang, H. Ran, Y. Zheng, D. Wang, J. Xu, and al, Nanoparticle-enhanced synergistic  
648 HIFU ablation and transarterial chemoembolization for efficient cancer therapy. *Nanoscale* 8 (2016)  
649 4324–39.
- 650 8. M. Bañobre-López, A. Teijeiro, J. Rivas, Magnetic nanoparticle-based hyperthermia for cancer  
651 treatment. *Reports of Practical Oncology & Radiotherapy* 18 (2013) 397-400.
- 652 9. A. Jordan, R. Scholz, K. Maier-Hauff, F.K.H.V. Landeghem, N. Waldoefner, U. Teichgraber,  
653 and al, The effect of thermotherapy using magnetic nanoparticles on rat malignant glioma. *J*  
654 *Neurooncol.* 78 (2005) 7-14.
- 655 10. J.A. Schwartzbaum, J.L. Fisher, K.D. Aldape, M. Wrensch, Epidemiology and molecular  
656 pathology of glioma. *Nature Clinical Practice Neurology* 2 (2006) 494–503.
- 657 11. UK CR. Types of primary brain tumors. Last accessed 13 August 2009 at  
658 <http://www.cancerhelp.org.uk/help/default.asp?page=5014>
- 659 12. Q.T. Ostrom, L. Bauchet, F.G. Davis, I. Deltour, J.L. Fisher, C.E. Langer, and al, The  
660 epidemiology of glioma in adults: a “state of the science” review. *Neuro Oncol.* 16 (2014) 896–913.
- 661 13. R. Stupp, M.E. Hegi, W.P. Mason, M.J. van den Bent, M.J. Taphoorn, R.C. Janzer, and al,  
662 Effects of radiotherapy with concomitant and adjuvant temozolomide versus radiotherapy alone on  
663 survival in glioblastoma in a randomised phase III study: 5-year analysis of the EORTC-NCIC trial. *The*  
664 *Lancet Oncology* 10 (2009) 459–66.
- 665 14. C. Billecke, S. Finnis, L. Tahash, C. Miller, T. Mikkelsen, N.P. Farrell, and al., Polynuclear  
666 platinum anticancer drugs are more potent than cisplatin and induce cell cycle arrest in glioma. *Neuro-*  
667 *oncol* 8 (2006) 215–26.

- 668 15. H.H. Ross, M. Rahman, L.H. Levkoff, S. Millette, T. Martin-Carreras, E.M. Dunbar, and al.,  
669 Ethynyldeoxyuridine (EdU) suppresses in vitro population expansion and in vivo tumor progression of  
670 human glioblastoma cells. *J Neurooncol.* 105 (2011) 485–98.
- 671 16. F-Y. Yang, M-C. Teng, M. Lu, H-F. Liang, Y-R. Lee, C-C. Yen, and al., Treating glioblastoma  
672 multiforme with selective high-dose liposomal doxorubicin chemotherapy induced by repeated focused  
673 ultrasound. *Int J Nanomedicine* 7(2012) 965–74.
- 674 17. F. Safdie, S. Brandhorst, M. Wei, W. Wang, C. Lee, S. Hwang, and al., Fasting Enhances the  
675 Response of Glioma to Chemo- and Radiotherapy. *PLOS ONE* 7 (2012) e44603.
- 676 18. G.L. Bidwell, E. Perkins, J. Hughes, M. Khan, J.R. James, D. Raucher, Thermally Targeted  
677 Delivery of a c-Myc Inhibitory Polypeptide Inhibits Tumor Progression and Extends Survival in a Rat  
678 Glioma Model. *PLOS ONE* 8. (2013) e55104.
- 679 19. W.L. Tittsworth, G.J.A. Murad, B.L. Hoh, M. Rahman, Fighting Fire with Fire: The Revival of  
680 Thermo-therapy for Gliomas. *Anticancer Res.* 34 (2014) 565–74.
- 681 20. F. Jiang, X. Zhang, S.N. Kalkanis, Z. Zhang, H. Yang, M. Katakowski, and al., Combination  
682 Therapy with Antiangiogenic Treatment and Photodynamic Therapy for the Nude Mouse Bearing U87  
683 Glioblastoma. *Photochem Photobiol.* 84 (2008) 128–37.
- 684 21. I. Rabias, D. Tsi-trouli, E. Karakosta, T. Kehagias, G. Diamantopoulos, M. Fardis, and al., Rapid  
685 magnetic heating treatment by highly charged maghemite nanoparticles on Wistar rats exocranial glioma  
686 tumors at microliter volume. *Biomicrofluidics.* 4 (2010) 024111.
- 687 22. M. Shinkai, M. Yanase, M. Suzuki, H. Honda, T. Wakabayashi, J. Yoshida, and al., Intracellular  
688 hyperthermia for cancer using magnetite cationic liposomes. *Journal of Magnetism and Magnetic*  
689 *Materials.* 194 (1999) 176–84.

- 690 23. A. Ito, M. Shinkai, H. Honda, T. Kobayashi, Heat-inducible TNF-alpha gene therapy combined  
691 with hyperthermia using magnetic nanoparticles as a novel tumor-targeted therapy. *Cancer Gene Ther.* 8  
692 (2001) 649–54.
- 693 24. T. Ohno, T. Wakabayashi, A. Takemura, J. Yoshida, A. Ito, M. Shinkai, and al., Effective  
694 Solitary Hyperthermia Treatment of Malignant Glioma Using Stick Type CMC-magnetite. *In vivo*  
695 Study. *J Neurooncol.* 56 (2002) 233–9.
- 696 25. B. Le, M. Shinkai, T. Kitade, H. Honda, J. Yoshida, T. Wakabayashi, and al., Preparation of  
697 Tumor-Specific Magnetoliposomes and Their Application for Hyperthermia. *Journal of Chemical*  
698 *Engineering of Japan.* 34 (2001) 66–72.
- 699 26. K. Maier-Hauff, R. Rothe, R. Scholz, U. Gneveckow, P. Wust, B. Thiesen, and al., Intracranial  
700 thermotherapy using magnetic nanoparticles combined with external beam radiotherapy: results of a  
701 feasibility study on patients with glioblastoma multiforme. *J Neurooncol.* 81 (2007) 53–60.
- 702 27. K. Maier-Hauff, F. Ulrich, D. Nestler, H. Niehoff, P. Wust, B. Thiesen, and al., Efficacy and  
703 safety of intratumoral thermotherapy using magnetic iron-oxide nanoparticles combined with external  
704 beam radiotherapy on patients with recurrent glioblastoma multiforme. *J Neurooncol.* 103 (2011) 317–  
705 24.
- 706 28. E. Alphandéry, S. Faure, O. Seksek, F. Guyot, I. Chebbi, Chains of Magnetosomes Extracted  
707 from AMB-1 Magnetotactic Bacteria for Application in Alternative Magnetic Field Cancer Therapy.  
708 *ACS Nano.* 5 (2011) 6279–96.
- 709 29. E. Alphandéry, F. Guyot, I. Chebbi, Preparation of chains of magnetosomes, isolated from  
710 *Magnetospirillum magneticum* strain AMB-1 magnetotactic bacteria, yielding efficient treatment of  
711 tumors using magnetic hyperthermia. *International Journal of Pharmaceutics.* 434 (2012) 444–52.

- 712 30. E. Alphandéry, M. Amor, F. Guyot, I. Chebbi, The effect of iron-chelating agents on  
713 *Magnetospirillum magneticum* strain AMB-1: Stimulated growth and magnetosome production and  
714 improved magnetosome heating properties. *Applied Microbiology and Biotechnology*. 96 663–70.
- 715 31. E. Alphandéry, S. Faure, L. Raison, E. Duguet, P.A. Howse, D.A. Bazylinski, Heat Production  
716 by Bacterial Magnetosomes Exposed to an Oscillating Magnetic Field. *J Phys Chem C*. 115 (2011) 18–  
717 22.
- 718 32. E. Alphandéry, I. Chebbi, F. Guyot, M. Durand-Dubief, Use of bacterial magnetosomes in the  
719 magnetic hyperthermia treatment of tumours: A review. *International Journal of Hyperthermia*. 29  
720 (2013) 801–9.
- 721 33. E. Alphandéry, Applications of Magnetosomes Synthesized by Magnetotactic Bacteria in  
722 Medicine. *Front Bioeng Biotechnol*. 11 (2014) 2:5.
- 723 34. D.E. Bordelon, C. Cornejo, C. Grüttner, F. Westphal, T.L. DeWeese, R. Ivkov, Magnetic  
724 nanoparticle heating efficiency reveals magneto-structural differences when characterized with wide  
725 ranging and high amplitude alternating magnetic fields. *Journal of Applied Physics*. 109 (2011) 124904.
- 726 35. C. Grüttner, K. Müller, J. Teller, F. Westphal, A. Foreman, R. Ivkov, Synthesis and antibody  
727 conjugation of magnetic nanoparticles with improved specific power absorption rates for alternating  
728 magnetic field cancer therapy. *Journal of Magnetism and Magnetic Materials*. 311 (2007) 181–6.
- 729 36. K. Cui, X. Xu, H. Zhao, S.T.C. Wong, A quantitative study of factors affecting in vivo  
730 bioluminescence imaging. *Luminescence*. 23 (2008) 292–5.
- 731 37. A. Sun, L. Hou, T. Prugpichailers, J. Dunkel, M.A. Kalani, X. Chen, and al., Firefly luciferase-  
732 based dynamic bioluminescence imaging: a noninvasive technique to assess tumor angiogenesis.  
733 *Neurosurgery*. 66 (2010) 751–757.

- 734 38. R. Hashizume, T. Ozawa, E.B. Dinca, A. Banerjee, M.D. Prados, C.D. James, and al., A human  
735 brainstem glioma xenograft model enabled for bioluminescence imaging. *J Neurooncol.* 96 (2010) 151–  
736 9.
- 737 39. E.B. Dinca, J.N. Sarkaria, M.A. Schroeder, B.L. Carlson, R. Voicu, N. Gupta, and al.,  
738 Bioluminescence monitoring of intracranial glioblastoma xenograft: response to primary and salvage  
739 temozolomide therapy. *J Neurosurg.* 107 (2007) 610–6.
- 740 40. O. Szentirmai, C.H. Baker, N. Lin, S. Szucs, M. Takahashi, S. Kiryu, and al., Noninvasive  
741 Bioluminescence Imaging of Luciferase Expressing Intracranial U87 Xenografts: Correlation with  
742 Magnetic Resonance Imaging Determined Tumor Volume and Longitudinal Use in Assessing Tumor  
743 Growth and Antiangiogenic Treatment Effect. *Neurosurgery.* 58 (2006) 365-372.
- 744 41. H. Zhou, K. Luby-Phelps, B.E. Mickey, A.A. Habib, R.P. Mason, D. Zhao, Dynamic Near-  
745 Infrared Optical Imaging of 2-Deoxyglucose Uptake by Intracranial Glioma of Athymic Mice. *PLOS*  
746 *ONE.* 4 (2009) e8051.
- 747 42. D.F. Heitjan, A. Manni, R.J. Santen, Statistical analysis of in vivo tumor growth experiments.  
748 *Cancer Res.* 53 (1993) 6042–50.
- 749 43. S-J. Kim, H.J. Lee, M.S. Kim, H.J. Choi, J. He, Q. Wu, et al., Macitentan, a Dual Endothelin  
750 Receptor Antagonist, in Combination with Temozolomide Leads to Glioblastoma Regression and Long-  
751 term Survival in Mice. *Clin Cancer Res.* 21 (2015) 4630–41.
- 752 44. E. Alphandéry, A.T. Ngo, C. Lefèvre, I. Lisiecki, L.F. Wu, M.P. Pileni. Difference between the  
753 Magnetic Properties of the Magnetotactic Bacteria and Those of the Extracted Magnetosomes: Influence  
754 of the Distance between the Chains of Magnetosomes. *J Phys Chem C.* 112 (2008) 12304–9.
- 755 45. D.A. Bazylinski, R.B. Frankel, Magnetosome formation in prokaryotes. *Nat Rev Micro.* 2 (2004)  
756 217–30.

- 757 46. L.C. Branquinho, M.S. Carrião, A.S. Costa, N. Zufelato, M.H. Sousa, R. Miotto, and al., Effect  
758 of magnetic dipolar interactions on nanoparticle heating efficiency: Implications for cancer  
759 hyperthermia. *Scientific Reports*. 3 (2013) 2887.
- 760 47. C. Grüttner, K. Müller, J. Teller, F. Westphal, A. Foreman, R. Ivkov, Synthesis and antibody  
761 conjugation of magnetic nanoparticles with improved specific power absorption rates for alternating  
762 magnetic field cancer therapy. *Journal of Magnetism and Magnetic Materials*. 311 (2007) 181–6.
- 763 48. C.R. Casella, T.C. Mitchell, Putting endotoxin to work for us: monophosphoryl lipid A as a safe  
764 and effective vaccine adjuvant. *Cell Mol Life Sci*. 65 (2008) 3231–40.
- 765 49. M.E. Astiz, E.C. Rackow, J.G. Still, S.T. Howell, A. Cato, K.B. Von Eschen, and al.,  
766 Pretreatment of normal humans with monophosphoryl lipid A induces tolerance to endotoxin: a  
767 prospective, double-blind, randomized, controlled trial. *Crit Care Med*. 23 (1995) 9–17.
- 768 50. Y. Liu, J. Wang, Effects of DMSA-Coated Fe<sub>3</sub>O<sub>4</sub> Nanoparticles on the Transcription of Genes  
769 Related to Iron and Osmosis Homeostasis. *Toxicol Sci*. 131 (2013) 521–36.
- 770 51. A. Tomitaka, Y. Takemura, Measurement of Specific Loss Power from Intracellular Magnetic  
771 Nanoparticles for Hyperthermia. *J Personali NanoMedicine*. 1 (2015) 33-37.
- 772 52. D.A. Bazylinski, R.B. Frankel, Magnetosome formation in prokaryotes. *Nat Rev Micro*. 2 (2004)  
773 217–30.
- 774 53. M. Creixell, A.C. Bohórquez, M. Torres-Lugo, C. Rinaldi, EGFR-Targeted Magnetic  
775 Nanoparticle Heaters Kill Cancer Cells without a Perceptible Temperature Rise. *ACS Nano*. 5 (2011)  
776 7124–9.
- 777 54. Z. Chen, W. Jalabi, K.B. Shpargel, K.T. Farabaugh, R. Dutta, X. Yin, and al.,  
778 Lipopolysaccharide-Induced Microglial Activation and Neuroprotection against Experimental Brain  
779 Injury Is Independent of Hematogenous TLR4. *J Neurosci*. 32 (2012) 11706–15.

- 780 55. T. Mentzel, L.F. Brown, H.F. Dvorak, C. Kuhnen, K.J. Stiller, D. Katenkamp, and al., The  
781 association between tumor progression and vascularity in myxofibrosarcoma and myxoid/round cell  
782 liposarcoma. *Virchows Arch.* 438 (2001) 13–22.
- 783 56. L. Asín, G.F. Goya, A. Tres, M.R. Ibarra, Induced cell toxicity originates dendritic cell death  
784 following magnetic hyperthermia treatment. *Cell Death Dis.* 4 (2013) e596.
- 785 57. F. Eriksson, P. Tsagozis, K. Lundberg, R. Parsa, S.M. Mangsbo, M.A.A. Persson, and al.,  
786 Tumor-Specific Bacteriophages Induce Tumor Destruction through Activation of Tumor-Associated  
787 Macrophages. *J Immunol.* 182 (2009) 3105–11.
- 788 58. J. Liang, Y. Piao, L. Holmes, G.N. Fuller, V. Henry, N. Tiao, and al., Neutrophils Promote the  
789 Malignant Glioma Phenotype through S100A4. *Clinical Cancer Research.* 20 (2014) 187–98.
- 790 59. A.W. Segal, How Neutrophils Kill Microbes. *Annu Rev Immunol.* 23 (2005) 197–223.
- 791 60. A.C. Silva, T.R. Oliveira, J.B. Mamani, S.M. Malheiros, L. Malavolta, L.F. Pavon, and al.,  
792 Application of hyperthermia induced by superparamagnetic iron oxide nanoparticles in glioma  
793 treatment. *Int J Nanomedicine.* 6 (2011) 591–603.
- 794 61. A. Jordan, R. Scholz, K. Maier-Hauff, F.K.H.V. Landeghem, N. Waldoefner, U. Teichgraeber,  
795 and al., The effect of thermotherapy using magnetic nanoparticles on rat malignant glioma. *J*  
796 *Neurooncol.* 78 (2006) 7–14.
- 797 62. K.F. Chu, D.E. Dupuy, Thermal ablation of tumours: biological mechanisms and advances in  
798 therapy. *Nat Rev Cancer.* 14 (2014) 199–208.
- 799 63. D.C. Wang, Y. Zhang, H.Y. Chen, X.L. Li, L.J. Qin, Y.J. Li, H.Y. Zhang, S. Wang,  
800 Hyperthermia Promotes Apoptosis and Suppresses Invasion in C6 Rat Glioma Cells. *Asian Pacific*  
801 *Journal of Cancer Prevention.* 13 (2012) 3239–45.

- 802 64. A. Morlé, C. Garrido, O. Micheau, Hyperthermia restores apoptosis induced by death receptors  
803 through aggregation-induced c-FLIP cytosolic depletion. *Cell Death Dis.* 6 (2015) e1633.
- 804 65. M. Nikfarjam, V. Muralidharan, C. Christophi, Mechanisms of Focal Heat Destruction of Liver  
805 Tumors. *Journal of Surgical Research.* 127 (2005) 208–23.

806